Journal of Catalysis 271 (2010) 262–279

Contents lists available at ScienceDirect

Journal of Catalysis

journal homepage: www.elsevier.com/locate/jcat

Applying spatially resolved concentration and temperature measurements in a catalytic plate reactor for the kinetic study of CO methanation

Jan Kopyscinski, Tilman J. Schildhauer *, Frédéric Vogel, Serge M.A. Biollaz, Alexander Wokaun

General Energy Research Department, Paul Scherrer Institut, CH-5232 Villigen PSI, Switzerland

ARTICLE INFO

Article history:
Received 19 November 2009
Revised 29 January 2010
Accepted 2 February 2010
Available online 31 March 2010

Keywords:
Kinetics
Catalytic plate reactor
Spatially resolved measurements
Methanation
Water gas shift reaction

ABSTRACT

In this work, the successful application of spatially resolved measurements in an optically accessible catalytic plate reactor was demonstrated, which allows the detailed investigation of the reaction kinetics of the exothermic CO methanation reaction with high initial CO partial pressure. By means of a movable sampling capillary, the axial gas species concentration profiles over the catalyst plate were measured, and the catalyst surface temperature was determined simultaneously along the reactor through a quartz glass window by means of infrared thermography. A one-dimensional model of the catalytic plate reactor and a Bayesian approach were applied to estimate the kinetic model parameters of the proposed Langmuir–Hinshelwood rate expressions by comparing simulated and measured gas concentration profiles. The validity of using a computationally efficient one-dimensional model was proven by solving a two-dimensional model using the kinetic parameters determined with the one-dimensional model and by comparing the two results.

1. Introduction

Modeling and simulation of chemical reactors is advantageous as it allows to easily study the influence of the operation conditions on the reactor performance, while the experimental work is limited to validation experiments. A high quality of the model prediction can only be obtained if all relevant processes in a chemical reactor and their interactions are represented adequately. Besides hydrodynamics, heat and mass transfer, a proper description of the reaction kinetics is necessary. For strongly exothermic and fast reactions, the determination of accurate kinetic parameters can be a challenge, especially when these reactions are part of a reaction network. The complete hydrogenation of CO to methane, also known as methanation reaction, in the presence of higher CO concentrations is an example for such a system (Rx 1–3).

$$3H_2 + CO \leftrightarrow CH_4 + H_2O \quad \Delta H_R^0 = -206.28\ \text{kJ/mol} \tag{Rx1}$$

$$CO + H_2O \leftrightarrow CO_2 + H_2 \quad \Delta H_R^0 = -41.16\ \text{kJ/mol} \tag{Rx2}$$

$$2CO \leftrightarrow C + CO_2 \quad \Delta H_R^0 = -172.54\ \text{kJ/mol} \tag{Rx 3}$$

The methanation reaction, its thermodynamics, elementary mechanism, kinetics, and catalyst deactivation mechanisms have been investigated intensively since in 1902 Sabatier and Senderens [1] found that nickel and other metals (Ru, Rh, Pt, Fe, Co) catalyzed this reaction. Important findings are summarized in [2–7].

The heterogeneously catalyzed methanation is important in two main industrial applications: (1) removal of traces of CO in hydrogen-rich gases, i.e., for the ammonia synthesis and (2) conversion of synthesis gas to a methane-rich fuel with a high heating value, so called synthetic or substitute natural gas (SNG). In the latter case, the synthesis gas produced by the gasification of solid fuels may contain, besides high amounts of H_2 and CO, also CO_2, H_2O, CH_4, and higher hydrocarbons. Coal to SNG, developed in the 1960s to the mid 1980s, is an established industrial process, while recently a sustained effort has been made to convert biomass feedstock into SNG via biomass gasification followed by methanation of the synthesis gas [8].

Due to the high CO concentration, two other independent reactions (Rx 2) and (Rx 3) are important in the methanation of biomass-derived synthesis gas, besides reaction (Rx 1). If the stoichiometric ratio of the reactants H_2/CO is at least three or more, carbon monoxide reacts with hydrogen mainly to methane and water according to (Rx 1). However, producer gases from biomass gasifiers usually have an H_2/CO ratio between 0.3 and 2, which is too low for a high CO conversion and long catalyst lifetime. By means of the water gas shift reaction (WGS, (Rx 2)), the H_2/CO ratio can be adjusted by converting CO with H_2O to CO_2 and additional H_2. The Boudouard reaction (Rx 3) is of importance, since carbon on the catalyst surface can be considered as a necessary intermediate during the methanation reaction but can also lead to catalyst deactivation [9,10]. Methane can also be formed by hydrogenation of carbon oxides in two other reactions ((Rx 4) and (Rx 5)).

* Corresponding author.
E-mail address: tilman.schildhauer@psi.ch (T.J. Schildhauer).

0021-9517/$ - see front matter © 2010 Elsevier Inc. All rights reserved.
doi:10.1016/j.jcat.2010.02.008

Nomenclature

a	specific surface area (m^{-1})
A	area (m^2)
b	width of the catalyst plate (m)
$c_{b,i}$	bulk gas concentration of species i (mol m^{-3})
$c_{s,i}$	concentration on the catalyst surface of species i (mol m^{-3})
Ca	Carberry number (–)
D_{ij}	binary diffusion coefficient (m^2 s^{-1})
$D_{eff,i}$	effective diffusion coefficient (m^2 s^{-1})
$D_{i,mix}$	diffusion coefficient of species i in the gas mixture (m^2 s^{-1})
$D_{K,i}$	Knudsen diffusion coefficient of species i (m^2 s^{-1})
Da_{II}	Damköhler number (–)
d_P	particle diameter (m)
d_{pore}	pore diameter (m)
E_A	activation energy (kJ mol^{-1})
ΔH_i	adsorption enthalpy of species i (kJ mol^{-1})
$h(x_i)$	catalyst height in interval i (m)
H	height of the channel (m)
K_{Gi}	mass transfer coefficient of species i (m s^{-1})
K_{eq}	equilibrium constant of the water gas shift reaction (–)
K_i	adsorption constant of species i (differ)
K_i^0	pre-exponential factor of the adsorption constant K_i (differ)
k_j	rate constant of reaction j (differ)
k_j^0	pre-exponential factor for rate constant k_j (differ)
l_{ch}	characteristic length (ratio of volume to surface) (m)
M_{av}	molar mass of gas mixture (g mol^{-1})
M_i	molar mass of species i (g mol^{-1})
m	catalyst mass (kg_{cat})
$\dot{n}_{b,i}$	molar flow of species i (mol s^{-1})
p_i	partial pressure of species i (bar)
$\Re$	universal gas constant = 8.314 (J mol^{-1} K^{-1})
r_j	rate of reaction 1, 2 (methanation and water gas shift, respectively) (mol kg_{cat}^{-1} s^{-1})
R_i	rate of disappearance or formation of species i (mol kg_{cat}^{-1} s^{-1})
Sh	Sherwood number (–)
T	temperature (K)
T_{ref}	reference temperature (598.15 K = 325 °C) (K)
u_{av}	average gas velocity (m s^{-1})
$u_x(h)$	axial gas velocity at height h (m s^{-1})
w_i	mass fraction of species i (–)
x_i	molar fraction of species i (–)
Δx_i	interval width (–)
x, y	co-ordinates (m)

Greek symbols

ε	void fraction or porosity (–)
η	catalyst effectiveness (–)
ρ	density (kg m^{-3})
$\theta_{E,j}$	dimensionless activation energy (–)
$\theta_{H,i}$	dimensionless heat of adsorption (–)
ω_{cat}	catalyst length density (kg_{cat} m^{-1})
Ψ	Weisz modulus (–)
Φ	Thiele modulus (–)
ϕ_P	particle sphericity (–)
τ	tortuosity (–)
ν_{ij}	stoichiometric factor (–)

$$2H_2 + 2CO \leftrightarrow CH_4 + CO_2 \quad \Delta H_R^0 = -247.44\ \text{kJ/mol} \qquad \text{(Rx4)}$$

$$4H_2 + CO_2 \leftrightarrow CH_4 + 2H_2O \quad \Delta H_R^0 = -165.12\ \text{kJ/mol} \qquad \text{(Rx 5)}$$

It has to be noticed that these reactions can be described as a linear combination of reactions (Rx 1) and (Rx 2). The CO_2 methanation (Rx 5) does not occur in the presence of CO [3], which could also be confirmed by experiments reported in this work (see Section 3.2).

In the past 50 years, more than 45 papers have been published regarding the kinetics of CO and CO_2 methanation, including the water gas shift reaction, over different nickel catalysts. However, in all of these studies only the gas composition at the reactor outlet for different experimental conditions was measured. By applying appropriate experimental conditions, the rate of the methanation reaction could be directly calculated from the conversion of CO or the exit gas concentration of CH_4. Most of the investigators used a flow reactor with gas recycle (i.e., Berty type) [11–16] or without gas recycle [17–28] to collect the kinetic data. To avoid an excessive temperature increase due to the exothermic reaction, highly diluted gas mixtures (>90% inert gas), and diluted catalyst beds were used, or the reactor was operated as a differential reactor with a very low CO conversion [20,27]. The flow reactors contained catalyst amounts of a few hundred milligrams up to several grams with particle sizes from several μm [19,22] up to 6 mm [11]. In some cases, the length of the catalyst bed was varied [25]. The problem with highly diluted gas mixtures and low CO conversions is the necessity to precisely measure CO and CH_4 in the ppmv range. Klose [11] reported an analytical error of 7% for CO and CH_4, and an even higher value for H_2, N_2, and CO_2. Another serious limitation of these systems for kinetic studies is the necessity to reach a gas composition at the exit that is sufficiently far away from chemical equilibrium.

While these studies relied on measuring the exit gas composition only, gathering information on gas composition and temperature profiles along the reactor axis allows the investigation of the reaction kinetics in much more detail. Spatially resolved measurements of gas species concentrations have already been applied in several studies for the partial oxidation of methane on a rhodium-coated foam at high temperature [29–33] and for the low temperature autothermal reforming of methane and gasoline using an earlier version of the catalytic plate reactor in our laboratory [34,35]. Here, a movable sampling capillary was used to acquire data along the reactor. Another possibility is the non-intrusive measurement of the gas composition by applying Raman and Laser Induced Fluorescence (LIF) techniques [36] in an optically accessible reactor.

In this study, we demonstrate the successful application of spatially resolved measurements in a catalytic plate reactor to investigate the influence of different parameters on the methanation reaction. The kinetic parameters were determined by comparing measured gas species concentration profiles with those derived from a one-dimensional reactor model. The kinetics validated by means of the one-dimensional modeling were applied into a two-dimensional model to verify the underlying assumption that the influence of film diffusion is negligible under the studied experimental conditions.

2. Experimental

2.1. Test rig

A test rig for the determination of kinetic parameters in heterogeneously catalyzed reactions designed by Bosco [35] was used. For studying the methanation reaction in the parameter space of

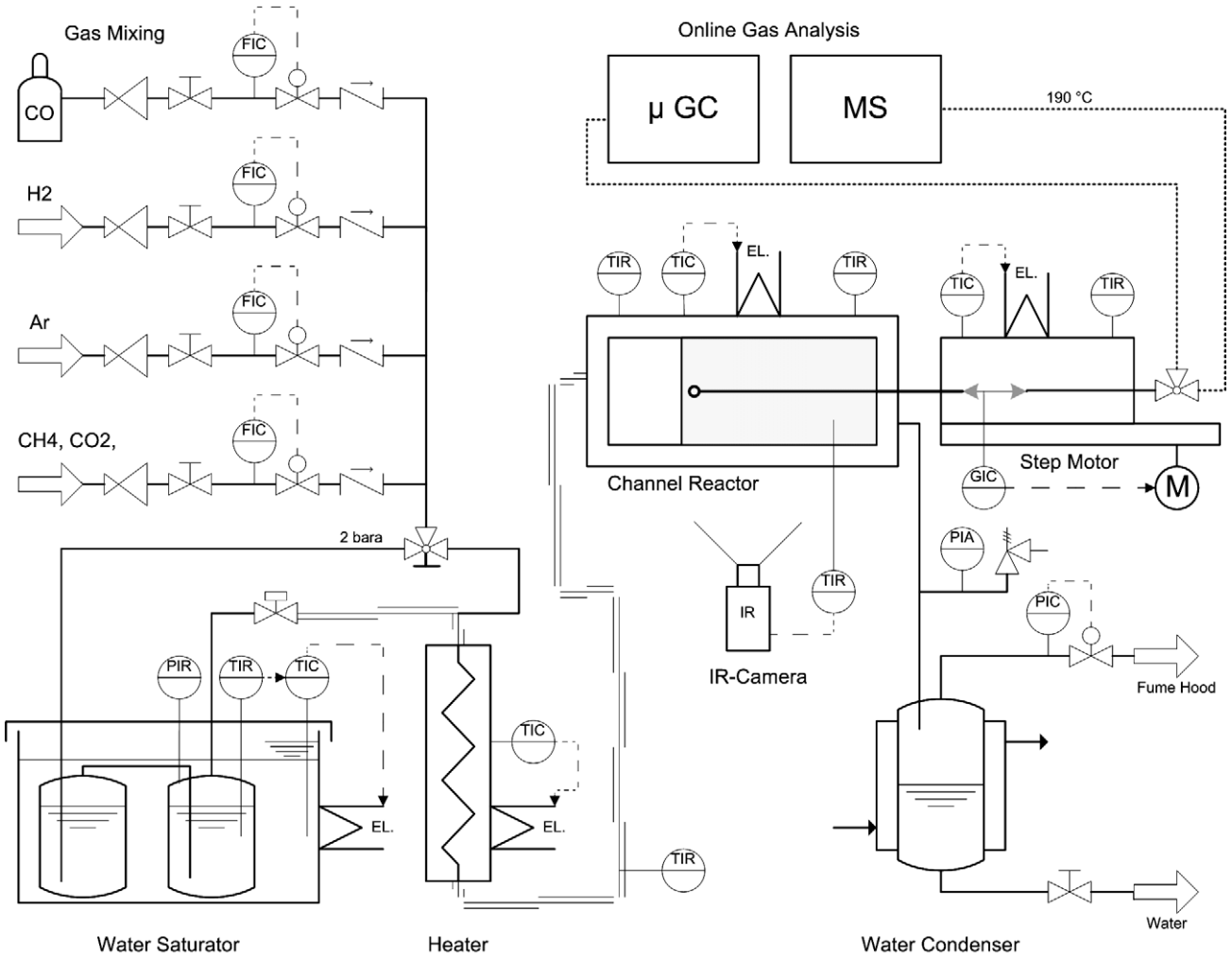

Fig. 1. Flow sheet of the catalytic plate reactor set-up.

interest, the setup had to be optimized in some aspects to assure the data quality necessary for the parameter estimation. The flow sheet is shown in Fig. 1. The setup consists of mass flow controllers, heated gas lines, and a water saturator for the supply of reactants, an optically accessible catalytic plate reactor, a gas-sampling and analysis section, and an infrared camera for measuring the temperature of the catalytic plate during the experiments. The reactant gases H_2, CO, CO_2, CH_4, and Ar were fed via calibrated mass flow controllers (Bronkhorst EL-Flow), and H_2O was added by passing the stream of reactant gases through a thermostatted saturator. The desired water content in the feed gas was achieved by adjusting the temperature of the saturator for a known system pressure. With this method, a constant mass flow of water without detectable fluctuations could be realized. The complete saturation is assured by applying two water tanks in series. The dry or wet feed gas was pre-heated and then introduced into the optically accessible catalytic plate reactor. The product gas was cooled to condense out the water and then sent to the fume hood.

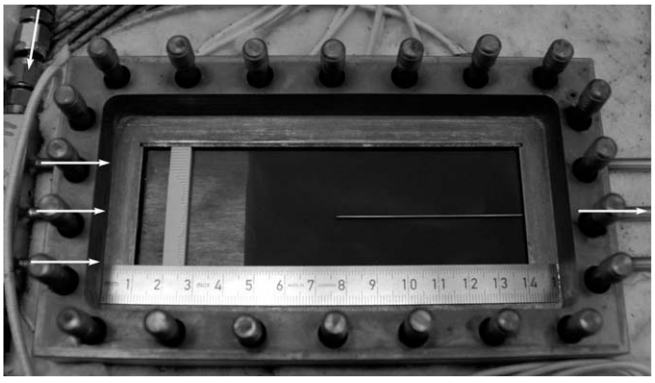

Fig. 2. Picture of the opened channel reactor with the catalyst plate installed, the flow straightener, and the movable sampling capillary.

2.2. Catalytic plate reactor

The catalytic plate reactor itself is a channel flow reactor in which a metal plate coated with a catalyst is placed and fixed at the bottom (see Fig. 2). The effective channel is 5 mm high, 50 mm wide, and 130 mm long, and its upper wall is a quartz glass plate (Herasil®).

The reactor is electrically heated using six heating cartridges placed in a massive stainless steel block under the metal plate. This allows a uniform temperature distribution over the whole channel area. A heated blower is used to heat the upper face of the quartz plate to assure temperature uniformity within 10 K over the height of the channel, i.e., in the space between the catalyst plate and the bottom face of the quartz glass. The earlier version of the channel reactor did not have this feature and exhibited temperature

gradients of up to 120 K over the gas channel, which had to be taken into account in the modeling. By avoiding such a large temperature difference, the modeling could be significantly simplified.

The catalyst surface temperature is determined by means of IR thermography. The digital IR camera Alpha NIR™ is sensitive in the near-infrared region (900–1680 nm) [37]. The quartz glass has a transmission of more than 90% for the wavelengths of 250–2000 nm [38]. We confirmed that the IR absorbing gas species did not have any influences on the temperatures measured by the IR camera.

Fig. 2 shows the opened channel reactor with the catalyst-coated plate installed. The reactants enter the reactor from the left via three inlet ports and pass over an uncoated area of the metal plate and through a piece of a monolith with 500-μm channels that serve as flow straightener. Approximately 20 mm after the flow straightener, the catalytically coated area begins. From the right hand side, a movable sampling capillary made of stainless steel is introduced into the channel through a high temperature septum port. The capillary with an external diameter of 0.8 mm is moved along the reactor axis by a linear positioning system (electric step motor controlled by LabVIEW™, accuracy < 0.1 mm). In this way, the local gas concentrations above the catalyst surface are measured online by a quadrupole mass spectrometer (QMS) connected to the capillary. The mass spectrometer (Pfeiffer Vacuum OmniStar GSD 301 O) has a Prisma™ ion source with an yttria-coated iridium cathode. The detector is a channeltron (CH-TRON) type secondary electron multiplier (SEM) and acquires mass spectra from 0 to 200 amu (atomic mass unit). The mass spectrometer operation and the data acquisition are computer controlled using the Quadstar 32-bit software. The QMS was calibrated for H_2 (2 amu), CO (28 amu), CO_2 (44 amu), CH_4 (15 amu), H_2O (18 amu), and Ar (40 amu). Argon was set as an internal standard. The contribution of the fragmentation of CO_2 to the CO signal at mass 28 was taken into account in the calibration.

The advantages of the optically accessible catalytic plate reactor are:

- measurement of the species concentration profiles in the gas channel along the reactor length by using a movable sampling capillary → high spatial resolution;
- spatially resolved measurement of the catalyst surface temperature by means of IR thermography;
- laminar flow in the gas channel → clearly defined mass transfer by pure diffusion in the direction normal to the catalyst plate;
- application of thin (<100 μm) catalyst coatings, reducing the importance of diffusional resistances within the catalyst coating;
- a high surface to volume ratio, producing only moderate hotspots even for highly exothermic reactions.

2.3. Catalyst preparation and characterization

The metal plate made from Fecralloy™ was coated with a commercial Ni–alumina catalyst (50 wt% Ni/Al_2O_3, BET = 183 m^2/g, all other data on the catalyst are confidential) as follows: At first, an aqueous dispersion of the catalyst powder (d_p < 45 μm) and a binder (Disperal®) was prepared. Prior to the coating, the Fecralloy-plate was calcined at 900 °C for more than 36 h to create a rough layer of alumina whiskers on the surface. Then the plate was coated with the catalyst suspension, dried, and calcined again at 420 °C for 4 h using a very low heating rate. Several mechanical and thermal tests were carried out to optimize the ratio of catalyst to binder for the coating, which was found to be 9:1. As shown in Fig. 2, not the complete metal plate was coated with the catalyst. Three coated metal plates with different catalyst loadings were used for the kinetic measurements as shown in Table 1.

Table 1
Coated metal plates used for the kinetic experiments.

	Catalyst mass (mg)	Coated area (mm^2)
Metal plate 1	246	93 × 48
Metal plate 2	225	93 × 48
Metal plate 3	57	73 × 48

The commercial nickel catalyst used is not promoted and does not contain significant amounts of Na and K. Due to this fact, the influence of catalyst promoters on the methanation reaction as described in the literature [39,6,40] is negligible.

Each catalyst plate was reduced inside the catalytic plate reactor at a temperature of 410 °C for 4 h with a constant flow of Ar and H_2. The concentration of H_2 was increased stepwise from 5 to 50 vol% and the H_2O evolution was measured to assure complete reduction of the nickel oxides, based on experience from temperature-programmed reduction experiments.

Since with the manual coating procedure it was not possible to distribute the catalyst evenly over the whole surface, the actual mass distribution had to be taken into account.

The height profiles of the coatings were measured to calculate the corresponding catalyst mass distribution along the coated area of the metal plate. The catalyst height was determined after the kinetic experiments by means of profilometry (Dektak 8 Stylus Profiler). The profiles were determined electromechanically by moving a diamond-tipped stylus over the sample. The stylus was mechanically coupled to a linear variable differential transformer (LVDT), which produced an analog signal proportional to the position change [41]. This signal was converted to a digital format for further processing.

2.4. Experimental conditions and procedure

The kinetic experiments were performed at five different temperatures from 280 to 360 °C at a total pressure of up to 2 bar_{abs}. Besides the influence of the hydrogen and carbon monoxide concentration, also the influence of the products methane, water, and carbon dioxide was investigated. The experimental conditions, valid for all five temperatures, are summarized in Table 2, i.e., up to 14 experiments were carried out per temperature.

Before the experiment, the reactor with the installed catalyst plate was heated up to the desired temperature under a constant flow of argon. The sampling capillary was moved to the zero position, approximately 1 mm after the flow straightener. Hydrogen was fed into the system, and the first IR line profile was recorded. Then CO, CO_2, and CH_4 were added stepwise until the desired volumetric flow rates were reached. The moving of the sampling capillary was started after the concentration at the zero position had reached a steady-state value. At this time, the second infrared line profile was recorded, and the temperature difference between the first and the second temperature profile was calculated.

The capillary was held for 45–180 s at each position and moved stepwise in flow direction to the end of the reactor. The volumetric flow rate through the capillary was measured to be between 3 and 10 ml_N/min, which corresponds to 1–3% of the total flow rate. In each (steady-state) experiment, up to 60 mass spectra were measured and averaged to determine the molar fractions at each axial position. Each run consisted of up to 40 capillary positions along the channel reactor.

After the profile measurements, the flows of CO, CO_2, and CH_4 were stopped and the capillary was moved to the zero position for the next run. Experiments containing water were carried out in a similar way, but all feed gases were fed through the water saturator.

Between the experiments, the reactor was flushed with a small flow of Ar containing 5 vol% H_2 in a temperature range of

Table 2
Experimental parameters for the CO methanation.

Exp. No.	Total flow (l_N/min)	Ar (mol%)	H_2 (mol%)	CO (mol%)	CO_2 (mol%)	CH_4 (mol%)	H_2O (mol%)	Ratio H_2/CO	Temperature (°C)
1	0.300	40.0	50.0	10.0	–	–	–	5	
2	0.300	28.0	60.0	12.0	–	–	–	5	
3	0.300	16.0	70.0	14.0	–	–	–	5	
4	0.450	30.0	60.0	10.0	–	–	–	6	
5	0.500	16.0	72.0	12.0	–	–	–	6	280,
6	0.400	35.0	50.0	10.0	5.0	–	–	5	300,
7	0.400	30.0	50.0	10.0	10.0	–	–	5	320,
8	0.400	35.0	50.0	10.0	–	5.0	–	5	340,
9	0.400	30.0	50.0	10.0	–	10.0	–	5	360
10	0.400	30.0	50.0	10.0	–	–	10.0	5	
11	0.400	25.0	50.0	10.0	–	5.0	10.0	5	
12	0.400	25.0	50.0	10.0	–	–	15.0	5	
13	0.400	15.0	50.0	10.0	–	10.0	15.0	5	
14	0.400	20.0	50.0	10.0	–	–	20.0	5	

300–340 °C to keep the catalyst in the reduced state. Every day, first the reference experiment no. 1 was performed. By comparing the concentration and temperature profiles of consecutive days, it was shown that catalyst deactivation was negligible.

Inside the sampling capillary, neither methanation nor water gas shift reactions occured. By conducting an experiment (no. 1) using an uncoated metal plate, it was shown that the hydrogen, carbon monoxide and argon concentrations do not change along the reactor axis. This can also be seen in Fig. 6, where the concentrations in the uncoated area (−20 to 0 mm) do not change.

3. Results

3.1. Catalytic coating

By measuring the catalyst height profile along the coated area of the metal plate, the catalyst mass in a given interval and the catalyst mass distribution ω_{cat} were calculated as follows:

$$\omega_{cat,\Delta x_i} = \frac{m_{\Delta x_i}}{\Delta x_i} = \frac{m_{cat}}{\sum h(x) \cdot \Delta x} \cdot h(x_i) \quad (1)$$

In Eq. (1), $m_{\Delta xi}$ is the catalyst mass in the considered interval in kg_{cat}, Δx_i is the interval width (distance between two capillary positions), m_{cat} is the total catalyst mass on the metal plate and $h(x_i)$ is the average catalyst height in the interval i.

An example of the height profile is shown in Fig. 3a. Five line scans were measured per catalyst plate, and all profiles show similar features. The beginning and the end of the coated area have more catalyst (thickness ca. 100 μm) than the part in the middle (20–50 μm).

The surface of the catalyst layer was comparatively rough-textured due to the catalyst particle size (d_P < 45 μm) used for the coating. The measurements confirmed that also the Fecralloy-plate had a relatively rough surface (approximately ±10 μm) after the first calcination procedure. The high amount of catalyst at the beginning and at the end of the plate can be explained by the fact that a tape was used to cover the part of the metal plate that should not be coated. The tape had a thickness of approximately 100 μm. Based on the line scans for one plate, a weighted average height in each interval was determined and by this the catalyst mass distribution, see Fig. 3b. By taking the height profile, the mass distribution along the coated area was then calculated and integrated into the reactor model.

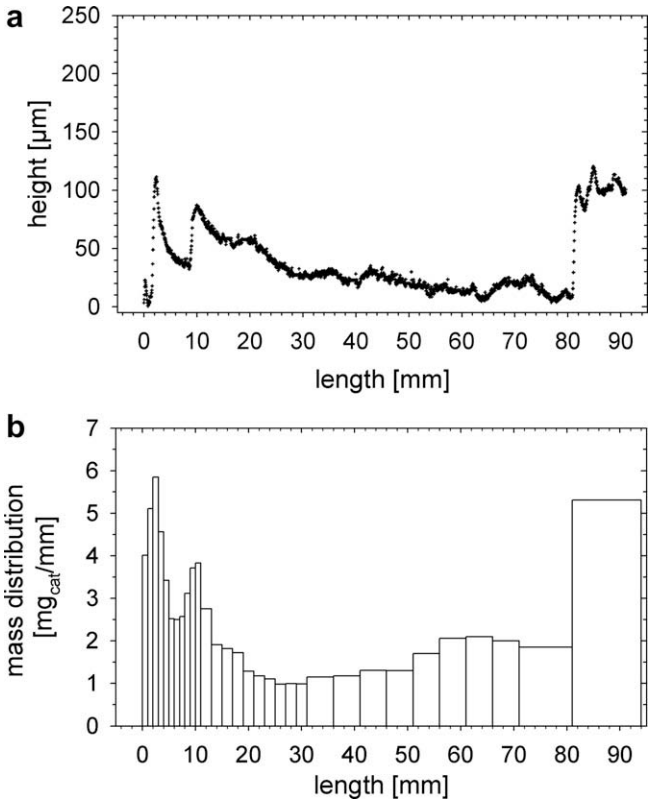

Fig. 3. (a) Measured height profile at centerline and (b) mass distribution of catalyst plate 1.

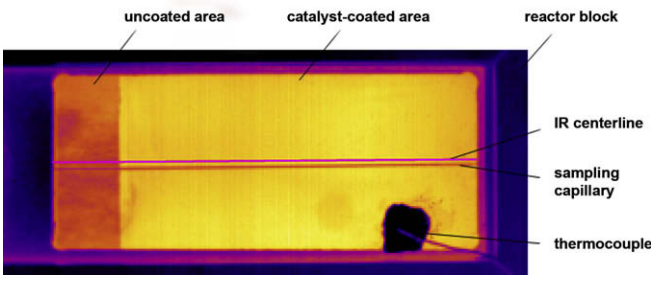

Fig. 4. Infrared picture obtained before CO was added to the gas stream (H_2, Ar) at 320 °C.

3.2. Concentration and temperature profiles

The catalyst surface temperature was recorded by means of IR thermography. A typical infrared picture obtained by the camera is depicted in Fig. 4; the brighter the color, the higher was the measured intensity. The camera was calibrated for the catalyst

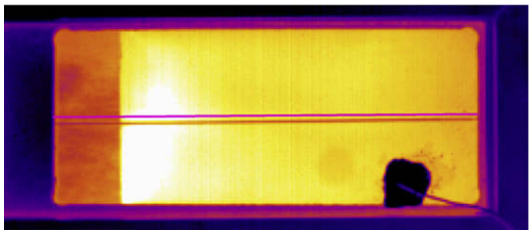

Fig. 5. Infrared picture during methanation at 320 °C (50 mol% H_2, 10 mol% CO, balance Ar).

surface, which has a different emissivity than the other parts (i.e., uncoated metal plate, reactor block, thermocouple, and sampling capillary). The dark blue area at the sides belongs to the reactor block. The uncoated area of the metal plate as well as the thermocouple on top of the quartz plate (fixed with aluminum tape) and the sampling capillary in the center of the reactor are visible. From the color gradient over the catalyst-coated area it can be seen that the temperature was evenly distributed, and that the inhomogeneities in the catalyst coating did not affect the temperature significantly. By means of the calibration, the surface temperature was calculated along the centerline (purple line next to the sampling capillary).

The IR picture in Fig. 4 was taken at a reactor temperature of 320 °C while the gas flow contained Ar and H_2 but no CO. By adding CO to the reactor feed stream, the exothermic methanation reaction started and a temperature increase was observed, as illustrated in Fig. 5 with a bright spot at the beginning of the catalyst-coated area.

3.2.1. Concentration profile at reference conditions

The gas species concentration and the catalyst temperature profiles for the reference condition $H_2/CO = 5$ (experiment no. 1 in Table 2) are plotted in Figs. 6–8 for 280, 320, and 360 °C, respectively. The catalyst-coated area begins at 0 mm, the 19 mm before that area are not coated with the catalyst. The upper part of the diagram illustrates the temperature difference ($T_{\text{with CO}} - T_{\text{without CO}}$) along the catalyst plate, while the graphs below show the gas concentrations of the species Ar, H_2, CO, CO_2, CH_4, and H_2O in vol%.

At 280 °C, H_2 and CO react to produce CH_4 and H_2O according to (Rx 1). The concentrations of H_2 and CO decrease from 50 vol% at the inlet to 30 vol% at the outlet, and from 10 vol% to 2 vol%, respectively. The gas concentrations of CH_4 and H_2O are equal at each position along the plate and reach 9.2 and 9.4 vol% at the outlet, respectively. The presence of equimolar amounts of CH_4 and H_2O, and the fact that no CO_2 was formed means that the water gas shift reaction is negligible at 280 °C. The conversion of CO and H_2 were 82.6% and 48.4%, respectively. The increase of the Ar concentration is due to the volume contraction of about 17%.

The temperature profile indicates an almost constant temperature along the plate, with slightly higher values at the beginning and the end of the catalyst area. The CO profile shows a similar behavior: the slope for the first 5 mm is steeper, then it flattens, and in the last 10 mm, it is steeper again. Both effects are caused by the inhomogeneous distribution of the catalyst mass on the metal plate; see Fig. 3. The first and the last millimeters of the coated area have thicker catalyst layers and thus a higher catalyst mass per unit length. However, all profiles recorded on the same catalyst plate can be evaluated and compared with each other.

At higher temperatures, the rates of disappearance of CO and H_2 and the rate of formation of H_2O and CH_4 increase. At 320 °C, CO is

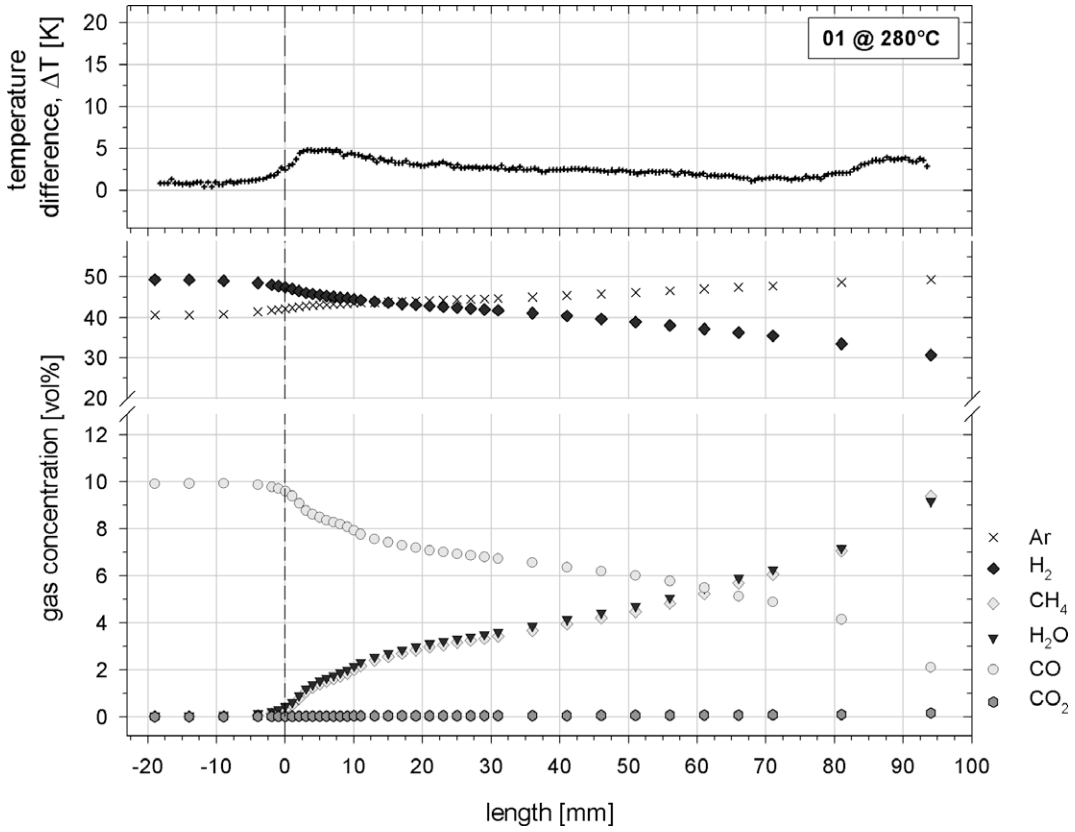

Fig. 6. Measured axial gas species concentration profiles and temperature difference of the reference experiment no. 1 ($H_2/CO = 5$) at 280 °C. (×) Ar, (♦) H_2, (◈) CH_4, (▼) H_2O, (○) CO, and (⬡) CO_2.

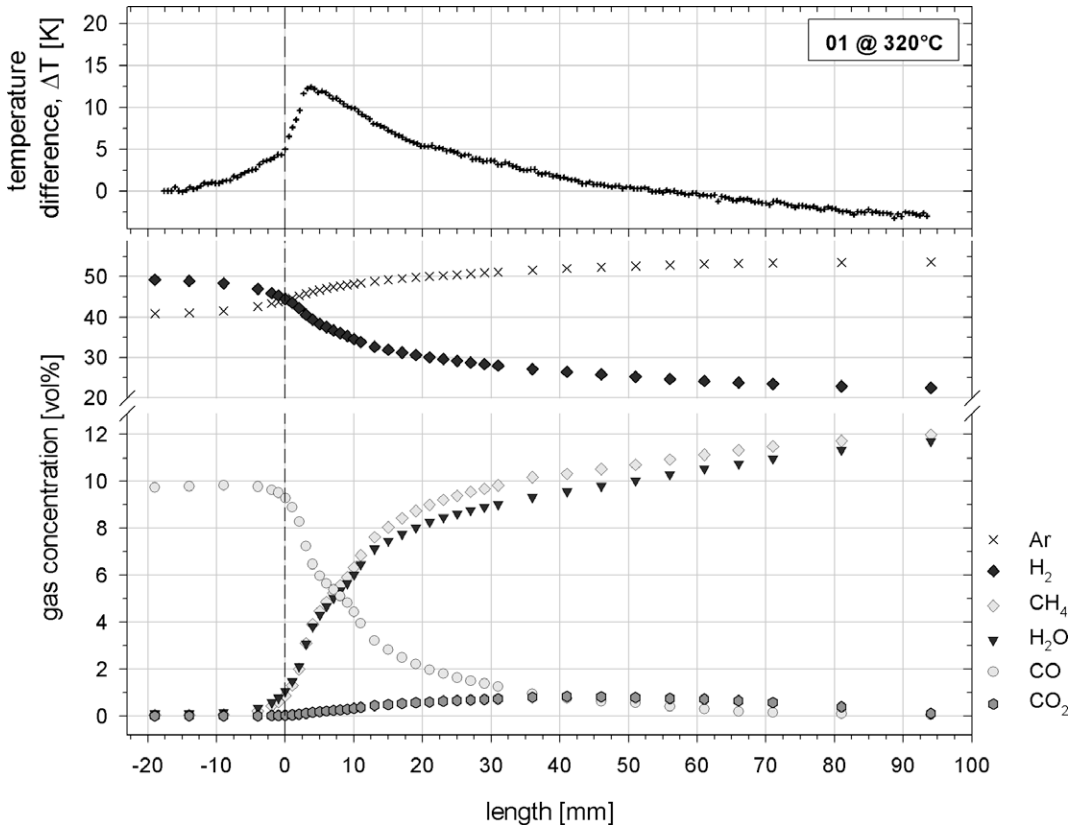

Fig. 7. Measured axial gas species concentration profiles and temperature difference of experiment no. 1 at 320 °C. (×) Ar, (♦) H_2, (◈) CH_4, (▼) H_2O, (◍) CO, and (⬢) CO_2.

completely converted at the end of the plate, and at 360 °C already after 80 mm, see Figs. 7 and 8. The concentrations of CH_4 and H_2O at the outlet reach almost the equilibrium concentration of 12.5 vol% for CH_4 and H_2O at 320–360 °C. The equilibrium composition calculated by means of the software HSC Chemistry 5.1 does not predict any CO_2 formation. However, the concentration profiles show at first an increase of CO_2, which then passes through a maximum and then decreases again. The increase of CO_2 is caused by the water gas shift reaction, which is accompanied by the consumption of water. It can be seen that the H_2O concentration is lower than the CH_4 concentration in this area where CO_2 reaches values of ca. 1 vol%. As soon as the CO concentration is below ca. 1 vol%, the CO_2 concentration decreases again. An explanation is as follows: up to ca. 10 mm, the conversion of CO is almost exclusively by hydrogenation to CH_4 and H_2O. As the concentration of H_2O increases, the water gas shift reaction becomes important and leads to the formation of small amounts of CO_2. The dominant route for CO conversion is still the methanation. When the concentration of CO reaches a level below the equilibrium value of the water gas shift, i.e., ca. 1 vol%, the reverse water gas shift reaction takes place because there is still a high concentration of H_2 present. This leads to a decrease in the CO_2 concentration and to an increase in the H_2O concentration to a value again equal to the CH_4 concentration at the end of the reactor. This observation confirms also the result that in the presence of CO the CO_2 methanation is inhibited [19]. The qualitative behavior is the same at 360 °C, although all reactions proceed faster.

Figs. 7 and 8 show a rapid temperature rise of 12 and 18 K, respectively, within the first 5 mm, which then declines with decreasing CO concentration. Here, the exothermicity of the methanation leads to a hotspot. Note that concentration data from axial positions within the hotspot have not been included for the determination of the kinetic parameters.

The atomic balances of C and O are for most experiments within 100 ± 5%, and just for a few cases outside the 100 ± 5% range, but always within 100 ± 10%. The hydrogen balances differ a bit more compared to that for carbon and oxygen; here, the atom balances were within 100 ± 10% for most of the experiments. For experiments with temperatures above 320 °C, the axially resolved hydrogen balance exhibited a few points that were between 100 ± 10% and 100 ± 15%. An explanation might be the increased axial dispersion of hydrogen at higher temperature. The plot of the atomic balances of C, O, and H along the reactor axis is depicted in the Supplementary material, see Fig. S1.

3.2.2. Effect of CO and H_2 partial pressures at $H_2/CO = 5$

Experiments nos. 2 and 3 (see Table 2) were conducted to investigate the influence of the CO and H_2 partial pressure for a constant H_2/CO ratio. The inlet concentrations were 50 vol% H_2 and 10 vol% CO for no. 1, 60 vol% H_2 and 12 vol% CO for no. 2, and 70 vol% H_2 and 14 vol% CO for experiment no. 3.

The rate of CO conversion and the rate of CH_4 and H_2O formation were calculated for each interval (distance between two capillary sampling positions) and compared with the reference experiment no. 1. The observed rates were computed by means of the measured concentration profile and the catalyst mass distribution, see Eq. (2).

$$\text{rate}_i = \frac{\dot{n}_i|_{x+\Delta x} - \dot{n}_i|_x}{m_{cat,\Delta x}} \tag{2}$$

Here $\dot{n}_i|_{x+\Delta x}$ is the molar flow (mol/s) of species i at the position $x + \Delta x$, $\dot{n}_i|_x$ is the molar flow at the position x, and $m_{cat,\Delta x}$ is the corresponding mass in the interval Δx. Fig. 9a and b illustrates the evolution of the observed rates for CO and CH_4 along the catalyst-coated area for the three experiments at 320 °C.

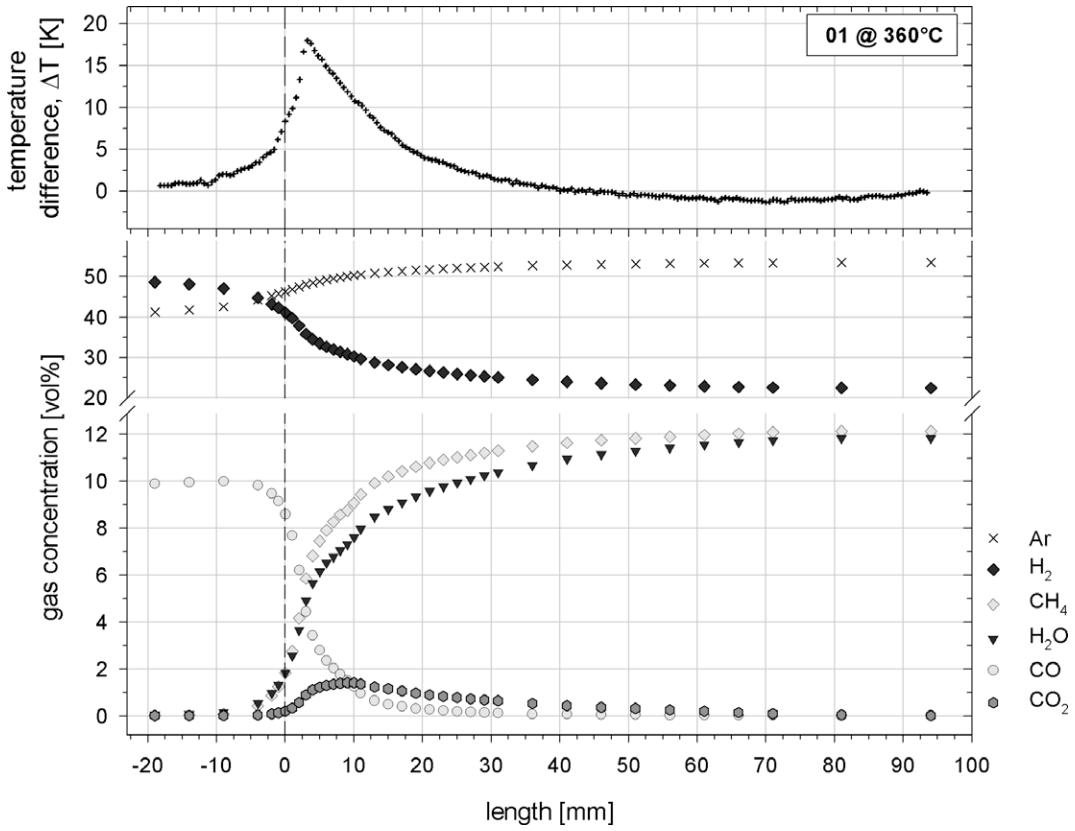

Fig. 8. Measured axial gas species concentration profiles and temperature difference of experiment no. 1 at 360 °C. (×) Ar, (♦) H_2, (◈) CH_4, (▼) H_2O, (◌) CO, and (⬡) CO_2.

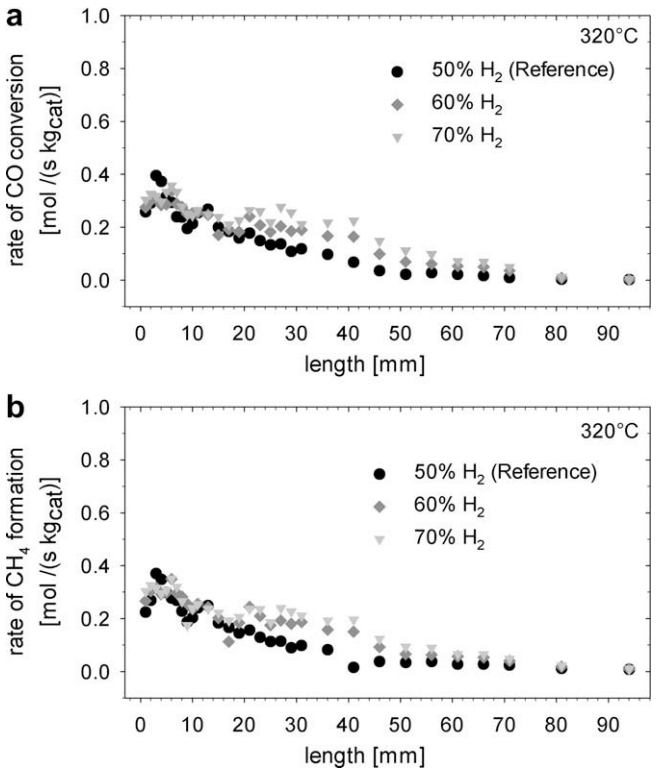

Fig. 9. Effect of H_2 partial pressure at constant H_2/CO ratio at 320 °C on the rates of (a) CO conversion and (b) CH_4 formation with (●) H_2 = 50%, (◈) H_2 = 60%, and (▼) H_2 = 70% in the feed, for experiment no. 1, 2, and 3, respectively.

The rate of CO conversion decreased from the beginning (position = 0 mm) to the end of the coated area. This might indicate a positive reaction order for CO. Furthermore, it can be seen that hydrogen did not influence significantly the reaction rates when varied between 50 and 70 vol%, because the rates of CO conversion and CH_4 formation of the three experiments were the same within experimental uncertainty. Also at temperatures higher than 320 °C neither retarding nor accelerating effects of hydrogen were observed. Only at 280 °C, a small accelerating influence of hydrogen was seen. This suggests that the reaction order of H_2 is close to zero or slightly positive.

3.2.3. Effect of CO_2

The influence of CO_2 on the methanation and water gas shift reactions was investigated by adding 5 mol% and 10 mol% of CO_2 to the reference mixture at temperatures from 280 to 360 °C. The corresponding experiment nos. are 1 for CO_2 = 0% (reference case), 6 for CO_2 = 5%, and 7 for CO_2 = 10% (see Table 2).

The concentration profiles for exp. nos. 6 and 7 (not shown) confirmed that the water gas shift and reverse water gas shift reaction are negligible at 280 °C.

Fig. 10 illustrates the evolution of the observed rates for CO along the catalyst-coated area for the three experiments. In the first 3 mm, the rates for CO conversion are between 0.13 and 0.16 mol s^{-} kg_{cat}^{-1} for all three experiments. Then the rate of CO declines asymptotically to 0.7 ± 0.1 mol s^{-} kg_{cat}^{-1} for all three experiments and all three species CO, CH_4, and H_2O (the rates for CH_4 are not shown). The rates for H_2O and CH_4 formation in the first 3 mm are between 0.09 and 0.12 mol s^{-} kg_{cat}^{-1} for all three experiments, which is slower compared to the CO rates. This might

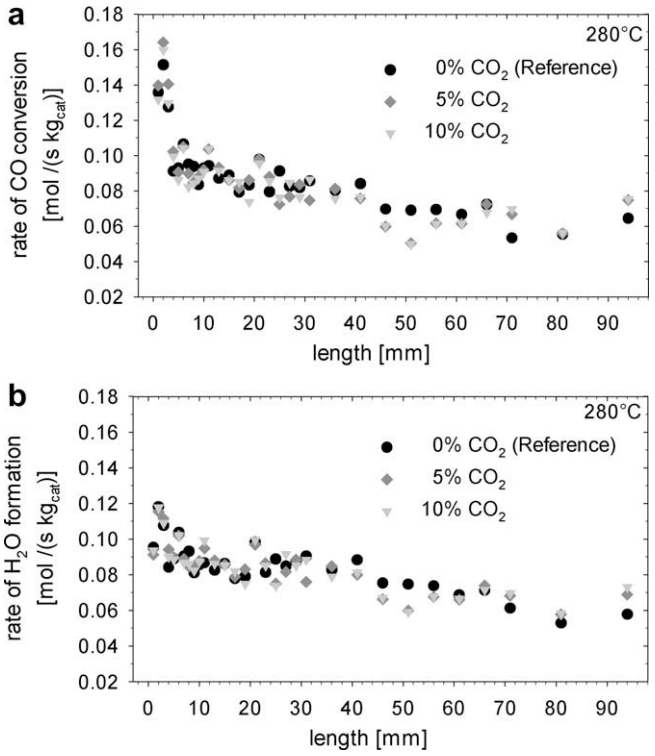

Fig. 10. Effect of CO_2 addition at 280 °C on the rates of (a) CO conversion and (b) H_2O formation with (●) CO_2 = 0%, (◆) CO_2 = 5%, and (▼) CO_2 = 10% in the feed, for experiment no. 1, 6, and 7, respectively.

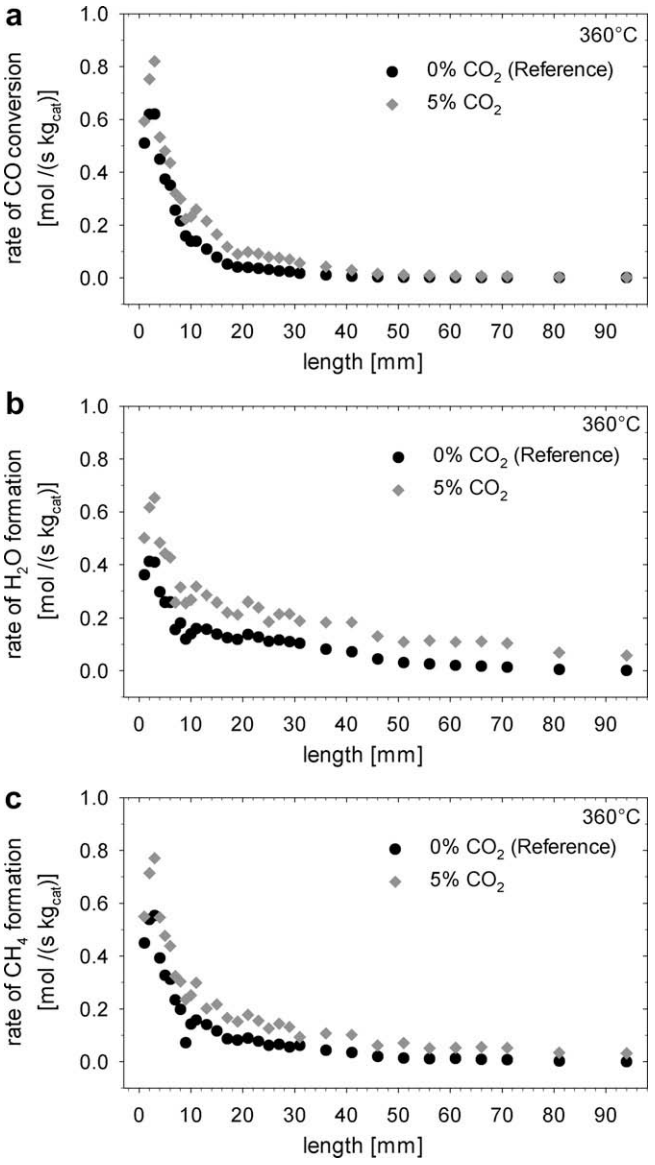

Fig. 11. Effect of CO_2 addition at 360 °C on the rates of (a) CO conversion, (b) H_2O and (c) CH_4 formation with (●) CO_2 = 0% and (◆) CO_2 = 5% in the feed, for experiment nos. 1 and 6, respectively.

suggest that not the CO adsorption is the limiting step, but rather one of the hydrogenation steps toward CH_4.

As a result, it can be concluded that CO_2 does neither affect the rate of CO conversion nor the ones of the production of H_2O and CH_4 at 280 °C. Also at higher temperatures, CO_2 does not retard the rate of CO conversion; it rather has a positive effect due to the reverse water gas shift producing additional CO, as it is depicted in Fig. 11. The rate of CH_4 formation increases as well by adding CO_2 to the feed. Furthermore, the rate of H_2O formation exceeds the CH_4 rate, because two moles of H_2O were produced instead of one mole of CH_4 by converting one mole of CO_2.

3.2.4. Effect of H_2O and CH_4

The effect of adding water and methane are depicted in Figs. 12 and 13 for 280 and 360 °C, respectively.

It can be seen that the rate of CO conversion was retarded by adding H_2O at 280 °C. The rates for CH_4 and H_2O are about the same as for the CO conversion and therefore the rate of H_2O is not shown here. This confirms that the water gas shift is negligible at temperatures below 300 °C.

With increasing temperature, the water gas shift and reverse water gas shift become more and more important; thus, the retarding effect of water decreases. Fig. 13a depicts the rate of CO conversion along the catalyst plate for the three cases at 360 °C. In the first 20 mm, the rates for CO are higher when adding water compared to the reference experiment. In contrary, the formation of water is slower within the first 20 mm compared to the reference experiment. But after 30 mm, the H_2O rate is slightly higher due to the reverse water gas shift, see Fig. 13b. For CH_4, the rate seems a bit higher with water over the complete range, see Fig. 13c. A further addition of methane (exp. no 11) did not affect the rates of CO, H_2O, and CH_4 at any temperature.

4. Reactor modeling and determination of kinetic parameters

4.1. Modeling the catalytic plate reactor

Modeling the catalytic plate reactor requires attention to several important aspects. Since the flow is laminar and bounded between two parallel plates, a parabolic velocity profile prevails throughout the channel. Moreover, the laminar flow allows transport by diffusion and thermal conduction only causing concentration and temperature gradients in the y-direction (channel height). Thus, the reaction might be limited by mass transfer from the bulk gas phase to the catalyst phase under certain conditions [42]. To model this kind of channel reactor, one- and two-dimensional model approaches are available [43]. The advantages and disadvantages are summarized in Table 3.

For the parameter estimation, a one-dimensional model was developed, which consists of a gas phase and a catalyst phase where the reactions take place. Both phases are connected through diffusive mass transport, which is described by the Sherwood

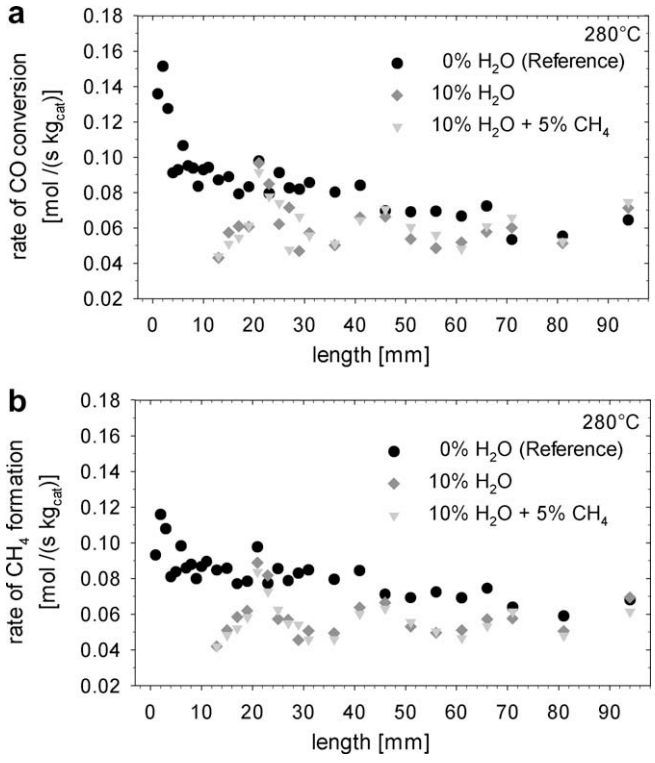

Fig. 12. Effect of H_2O and CH_4 addition on the rates of (a) CO conversion and (b) CH_4 formation with (●) H_2O = 0%, (◆) H_2O = 10%, and (▼) H_2O = 10% + CH_4 = 5% in the feed, for experiment nos. 1, 10, and 11, respectively at 280 °C.

correlation (*Sh*). The gas phase is computed as plug flow with a constant concentration and temperature in the *y*-direction. Thus, the one-dimensional model requires an average bulk concentration and an average bulk temperature; moreover an accurate correlation for the mass transfer from the bulk gas phase to the catalyst phase is necessary.

Since the temperature range for the methanation is between 280 and 380 °C, homogeneous gas phase reactions can be ignored and the reactions occur only on the catalyst surface. Further assumptions are made as follows:

- steady-state (no time dependence),
- ideal gas behavior,
- isothermal → no energy balance to be solved (only the isothermal part of the catalyst plate is modeled),
- no pressure loss → no momentum balance to be solved,
- catalyst mass distribution is taken into account,
- velocity change due to volume contraction is taken into account,
- no carbon deposition,
- catalyst layer is considered thin enough to neglect intraphase transport resistance,*
- average = measured gas concentration (one-dimensional model),*

*These assumptions were checked by applying a two-dimensional model and calculating the average gas concentration and the Weisz modulus.

The molar balance for species *i* in the bulk gas phase is

$$0 = -\frac{\partial \dot{n}_{b,i}}{\partial x} - b \cdot K_{G,i} \cdot (c_{b,i} - c_{s,i}) \tag{3}$$

and the molar balance for the surface is

$$0 = b \cdot K_{G,i} \cdot (c_{b,i} - c_{s,i}) + \omega_{cat} \cdot \sum_j \nu_{ij} \cdot r_j \tag{4}$$

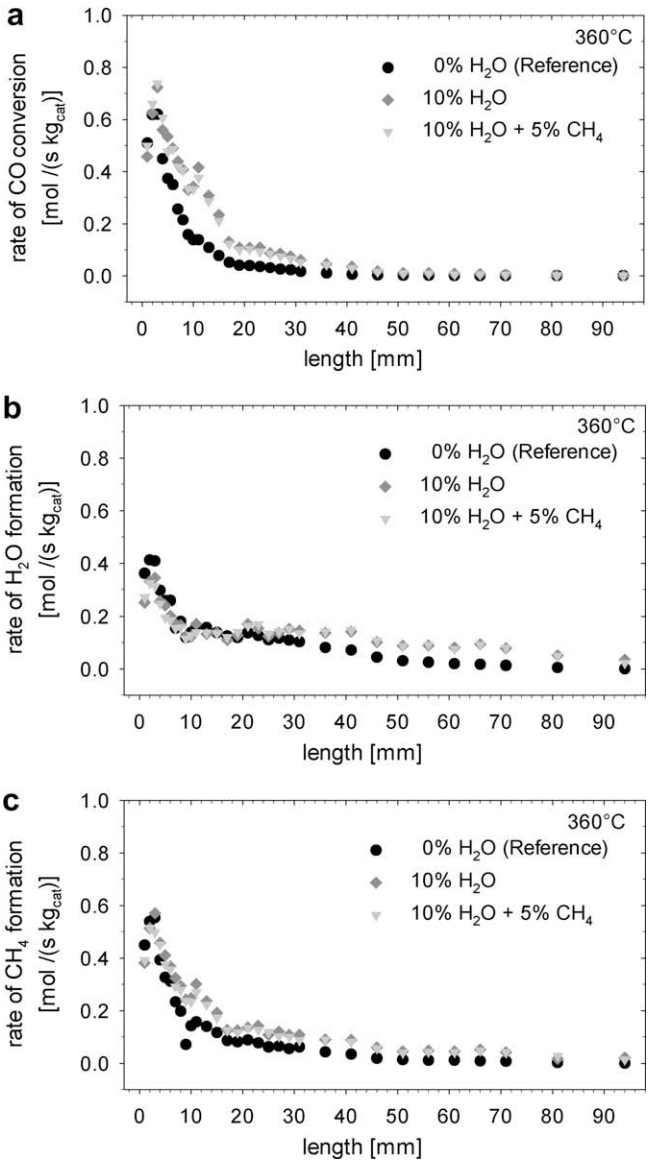

Fig. 13. Effect of H_2O and CH_4 addition on the rate of (a) CO conversion (b) rate of H_2O and (c) of CH_4 formation with (●) H_2O = 0%, (◆) H_2O = 10%, and (▼) H_2O = 10% + CH_4 = 5% in the feed, for experiment no. 1, 10, and 11, respectively at 360 °C.

where *b* (m) is the width of the channel, and the catalyst mass density along the plate is defined as ω_{cat} in $kg_{cat}\ m^{-1}$. The ratio between the convective and the diffusive mass transfer is expressed by the Sherwood number:

$$Sh = \frac{K_{G,i} \cdot l_{ch}}{D_{i,mix}} \tag{5}$$

A Sherwood number of 3.7 is used, as determined by Raja et al. [44] for catalytic combustion in a monolith reactor at low Reynolds numbers, with the height of the channel, H, as the corresponding characteristic length (l_{ch}). With Eq. (5), the molar balance for the bulk phase becomes

$$0 = -\frac{\partial \dot{n}_{b,i}}{\partial x} - b \cdot \frac{Sh \cdot D_{i,mix}}{H} \cdot (c_{b,i} - c_{s,i}) \tag{6}$$

and for the catalyst phase

$$0 = b \cdot \frac{Sh \cdot D_{i,mix}}{H} \cdot (c_{b,i} - c_{s,i}) + \omega_{cat} \cdot \sum_j \nu_{ij} \cdot r_j \tag{7}$$

Table 3
One-dimensional vs. two-dimensional model for channel reactors [42].

One-dimensional model	Two-dimensional model
• Two-phase model (bulk gas and species on catalyst) • average bulk concentration and temperature • only convection and diffusion in x-direction • no diffusion in y-direction • discontinuity at the catalyst surface • mass and heat transfer coefficients (Sh, Nu) are necessary • requires less computer time • useful for kinetic studies and parameter fitting	• Implements correctly the mass and heat flux boundary conditions • reaction implemented in the boundary condition • complex model • requires more computer time • no Sh and Nu correlation necessary: radial concentration and temperature gradients are calculated • useful for parametric studies

Table 4
Reaction mechanism A and B and possible rate-determining steps (RDS).

Mechanism A	Mechanism B	RDS	No.
	$H_2 + 2^* \leftrightarrow 2H^*$		R 1
	$CO + * \leftrightarrow CO^*$	X	R 2
$CO^* + * \leftrightarrow C^* + O^*$		X	R 3
	$CO^* + \alpha H^* \leftrightarrow COH^*_\alpha + \alpha^*$	X	R 4
	$COH^* + * \leftrightarrow CH^* + O^*$ or $C^* + OH^*$	X	R 5
	$COH^*_v + \alpha H^* \leftrightarrow COH^*_w + \alpha^*$	X	R 6
	$COH^*_x + \alpha H^* \leftrightarrow CH^*_y + OH^*_z$	X	R 7
$C^* + \alpha H^* \leftrightarrow CH^*_\alpha + \alpha^*$		X	R 8
$CH^* + H^* \leftrightarrow CH^*_2 + *$		X	R 9
$CH^*_2 + \alpha H^* \leftrightarrow CH^*_{2+\alpha} + \alpha^*$		X	R 10
$CH^*_3 + H^* \leftrightarrow CH^*_4 + *$			R 11
$CH^*_4 \leftrightarrow CH_4 + *$			R 12
$CO^* + O^* \leftrightarrow CO^*_2 + *$			R 13
$CO^*_2 \leftrightarrow CO_2 + *$			R 14
$O^* + H^* \leftrightarrow OH^* + *$			R 15
$OH^* + H^* \leftrightarrow H_2O^* + *$			R 16
$H_2O^* \leftrightarrow H_2O + *$			R 17
$CO^* + OH^* \leftrightarrow CO_2{}^* + H^*$			R 18
$CO^* + H_2O^* \leftrightarrow CO^*_2 + 2H^*$			R 19

$*$ Empty active site.
C^* adsorbed species (e.g., adsorbed carbon).
RDS rate-determining step.
$v = 1, 2$; $w = 2, 3$; $x = 1, 2, 3$; $y = 0, 1, 2$; $z = 0, 1, 2$; and $\alpha = 1, 2$.

The boundary conditions are defined as

$$\dot{n}_{b,i}|_{x=0} = \dot{n}_{b,i,feed} \quad \text{(initial condition } x = 0) \tag{8}$$

The molecular diffusion coefficient in the gas mixture is calculated with the method of Wilke [45], where the Fuller correlation was used for the binary diffusion coefficient [46].

$$D_{i,mix} = \frac{1 - x_i}{\sum_j x_j / D_{i,j}} \tag{9}$$

$$D_{i,j} = 0.01013 \cdot \frac{T^{1.75} \cdot \left(\frac{1}{M_i} + \frac{1}{M_j}\right)^{0.5}}{p \cdot \left[\left(\sum v_i\right)^{1/3} + \left(\sum v_j\right)^{1/3}\right]^2} \tag{10}$$

M_i is the molar weight of species i and v_i are the atomic diffusion volumes from [46].

4.2. Reaction mechanism and formulation of rate equations

As H_2 is present in excess and the reaction order of CO is greater than zero (see Figs. 9–13), it is assumed that adsorption of H_2 is in equilibrium. There is no consensus in the literature on the elementary steps for the methanation of CO on a nickel surface. Two different mechanisms have been proposed in the literature; both are summarized in Table 4 with possible assumed rate-determining steps (RDS).

Mechanism A is thought to proceed via molecular adsorption and subsequent dissociation of CO, steps R 2 and R 3. Adsorbed carbon (C^*) is assumed to be an intermediate, which reacts with hydrogen stepwise to methane (steps R 8–12). Mechanism A was proposed by Araki and Ponec in 1976 [47] and confirmed by other authors in experiments and calculations [11,22–24,48–55].

The different variants of mechanism B were mostly published in the 1970s and 1980s [14,19,20,39,56–58]. This mechanism proposes an oxygenated compound, e.g., a COH_x complex, as an intermediate. Recent DFT calculations and high-pressure experiments by Andersson et al. [59] support the picture that the methanation proceeds via a COH complex. It is assumed that in the presence of hydrogen, carbon monoxide does not dissociate, but rather reacts in the first state with hydrogen to form a COH_x complex (R 4), which then has a lower activation barrier for the C–O bond dissociation. This COH_x complex can either dissociate (R 5) or react via step R 6 or step R 7 to CH_y, which hydrogenates further to methane (step R 8–12). The values of x and y depend both on the experimental conditions and on the properties of the catalyst. Sanchez-Escribano et al. [60] further suggested from an IR-study on a Ni/Al_2O_3 catalyst that CO reacts with an adsorbed OH species to form a CH_3O adsorbate. This methoxy group reacts further with hydrogen to methane and a hydroxyl group.

The surface intermediates can either react with one adsorbed hydrogen atom (H^*), or with two adsorbed hydrogen atoms ($2H^*$). The reaction step in Table 4 changes accordingly.

The adsorption of hydrogen and carbon monoxide (R 1 and 2) and the hydrogenation of the CH_x complex (R 8–12) are common to both mechanisms.

Table 5
Parameters and exponents of the general rate equation for different RDS assumptions.

Model	RDS	K_{Cx}	a	b	c	K_{Cy}	e	f	g
1	$CO + *$	–	0	1.0	0	–	–	–	1
2	$CO^* + *$	K_{CO}	0	1.0	0	–	–	–	2
3	$CO^* + H^*$	K_{CO}	0.5	1.0	0.5	–	–	–	2
4	$CO^* + 2H^*$	K_{CO}	1.0	1.0	1.0	–	–	–	3
5	$COH^* + *$	K_{COH}	0	1.0	0.5	K_{COH}	1.0	0.5	2
6	$COH^* + H^*$	K_{COH}	0.5	1.0	1.0	K_{COH}	1.0	0.5	2
7	$COH^* + 2H^*$	K_{COH}	1.0	1.0	1.5	K_{COH}	1.0	0.5	3
8	$COH_2^* + H^*$	K_{COH_2}	0.5	1.0	1.5	K_{COH_2}	1.0	1.0	2
9	$COH_2^* + 2H^*$	K_{COH_2}	1.0	1.0	2.0	K_{COH_2}	1.0	1.0	3
10	$COH_3^* + H^*$	K_{COH_3}	0.5	1.0	2.0	K_{COH_3}	1.0	1.5	2
11	$COH_3^* + 2H^*$	K_{COH_3}	1.0	1.0	2.5	K_{COH_3}	1.0	1.5	3
12	$C^* + H^*$	K_C	0.5	0.5	0.5	K_C	0.5	0	2
13	$C^* + 2H^*$	K_C	1.0	0.5	1.0	K_C	0.5	0	3
14	$CH^* + H^*$	K_{CH}	0.5	0.5	1.0	K_{CH}	0.5	0.5	2
15	$CH_2^* + H^*$	K_{CH_2}	0.5	0.5	1.5	K_{CH_2}	0.5	1.0	2
16	$CH_2^* + 2H^*$	K_{CH_2}	1.0	0.5	2.0	K_{CH_2}	0.5	1.0	3

The attempt to formulate the rate equations follows the Langmuir–Hinshelwood approach using the assumption of a rate-determining step (RDS) for the proposed reaction mechanisms. This elementary step is considered the slowest reaction step and responsible for the overall rate. All other reaction steps are regarded to be in equilibrium or irreversible. The derivation of the rate equations takes the surface coverage of the relevant adsorbed species into account. With the different assumed rate-determining steps listed in Table 4, 16 models were derived and summarized in one generalized rate expression for the methanation reaction applying 16 different sets of exponents, see Table 5.

The rate equation for the methanation does not include the reverse reaction due to the very large equilibrium constant of $K_{p,Meth} = 7.8 \times 10^7$ bar^{-2} at 280 °C and 5.6×10^4 bar^{-2} at 380 °C. Below 380 °C, the equilibrium of the methanation reaction lies strongly on the side of the products; therefore, the reverse reaction (methane steam reforming) can be neglected.

The results of the kinetic experiments indicated that H_2O inhibits whereas CH_4 and CO_2 do not hinder the reaction rate; hence, the H_2O adsorption term was included in two different ways. If water adsorbs as an H_2O molecule, the rate becomes

$$r_1 = \frac{k_1 \cdot K_{Cx} \cdot K_{H_2}^a \cdot p_{CO}^b \cdot p_{H_2}^c}{\left(1 + \sqrt{K_{H_2} \cdot p_{H_2}} + K_{CO} \cdot p_{CO} + K_{H_2O} \cdot p_{H_2O} + K_{Cy} \cdot p_{CO}^e \cdot p_{H_2}^f\right)^g} \tag{11}$$

and if water adsorbs in the form of a hydroxyl species (OH), the rate equation changes to:

$$r_1 = \frac{k_1 \cdot K_{Cx} \cdot K_{H_2}^a \cdot p_{CO}^b \cdot p_{H_2}^c}{\left(1 + \sqrt{K_{H_2} \cdot p_{H_2}} + K_{CO} \cdot p_{CO} + K_{OH} \cdot p_{H_2O} \cdot p_{H_2}^{-0.5} + K_{Cy} \cdot p_{CO}^e \cdot p_{H_2}^f\right)^g} \tag{12}$$

where K_{Cx} and K_{Cy} denote the adsorption constants of the intermediate carbon species, which is a combination of an adsorption and a rate constant. The partial pressures p_i are expressed in bar and the reaction rate r_j in mol s^{-1} kg$_{cat}^{-1}$. The units of the rate constants and adsorption constants depend on the exponents used. Eqs. (11) and (12) show that adsorbed hydrogen, carbon monoxide, water or hydroxyl and an intermediate carbon species (C^*, CH_x^*, or COH_x^*) are assumed to be present on the surface. All coefficients of the rate equation are summarized in Table 5 for the different RDS assumed. Altogether these are 32 models, 16 models with an adsorbed H_2O (models 1a–16a) and 16 models with an adsorbed OH species (model 1b–16b).

The rate equation for the water gas shift also includes the reverse reaction, due to the small equilibrium constant ($K_{eq,WGS} = 55.2$ at 280 °C and $K_{eq,WGS} = 15.1$ at 380 °C) in the temperature range of interest. Since methanation and water gas shift are assumed to take place on the same sites, the denominator of the rate equations has to be the same [61]. For an adsorbed H_2O species, the WGS proceeds via step R 19 and the rate can be formulated as:

$$r_2 = \frac{k_2 \cdot \left(K_\beta \cdot p_{CO} \cdot p_{H_2O} - \frac{p_{CO_2} \cdot p_{H_2}}{K_{eq}}\right)}{\left(1 + \sqrt{K_{H_2} \cdot p_{H_2}} + K_{CO} \cdot p_{CO} + K_{H_2O} \cdot p_{H_2O} + K_{Cy} \cdot p_{CO}^e \cdot p_{H_2}^f\right)^2} \tag{13}$$

For an adsorbed OH species, the WGS proceeds via step R 18 and the rate can be formulated as

$$r_2 = \frac{k_2 \cdot \left(K_\alpha \cdot p_{CO} \cdot p_{H_2O} - \frac{p_{CO_2} \cdot p_{H_2}}{K_{eq}}\right)}{p_{H_2}^{0.5} \cdot \left(1 + \sqrt{K_{H_2} \cdot p_{H_2}} + K_{CO} \cdot p_{CO} + K_{OH} \cdot p_{H_2O} \cdot p_{H_2}^{-0.5} + K_{Cy} \cdot p_{CO}^e \cdot p_{H_2}^f\right)^2} \tag{14}$$

The coefficients K_α and K_β are a combination of the adsorption constant for CO, CO_2, H_2, and OH or H_2O. k_2 is a combination of the reaction constant of the water gas shift and the adsorption constants of the involved species. The equilibrium constant K_{eq} of the water gas shift was calculated directly from thermodynamic data taken from the DIPPR Project 801 database [62].

The reaction rates for the species H_2, CO, CH_4, CO_2, and H_2O were calculated using the following relations:

$$R_{H_2} = -3 \cdot r_1 + r_2 \tag{15}$$
$$R_{CO} = -r_1 - r_2 \tag{16}$$
$$R_{CH_4} = r_1 \tag{17}$$
$$R_{H_2O} = r_1 - r_2 \tag{18}$$
$$R_{CO_2} = r_2 \tag{19}$$

4.3. Parameter estimation

The parameters to be estimated were the pre-exponential factors of the rate and adsorption coefficients with the corresponding activation energies and heats of adsorption, which can be described by Arrhenius' and van't Hoff's equations, respectively, see Eqs. (20) and (21).

$$k_j = k_j^0 \cdot \exp\left\{-\frac{E_A}{\Re \cdot T}\right\} \tag{20}$$
$$K_i = K_i^0 \cdot \exp\left\{-\frac{\Delta H_i}{\Re \cdot T}\right\} \tag{21}$$

As this form of the equations often has huge magnitudes of k_j^0 and K_i^0, due to the fact that k_j^0 and K_i^0 refers to infinite temperature, a modified form based on a finite reference temperature T_{ref} is used. This temperature was set to 598.15 K (325 °C).

$$k_j = \exp\{\theta_{k,j}\} \cdot \exp\left\{\theta_{E,j}\left(1 - \frac{T_{ref}}{T}\right)\right\} \tag{22}$$
$$K_i = \exp\{\theta_{K,i}\} \cdot \exp\left\{\theta_{H,i}\left(1 - \frac{T_{ref}}{T}\right)\right\} \tag{23}$$

In Eqs. (22) and (23) the parameters are chosen to be $\theta_{k,i} = \ln(k_{j,T_{ref}})$ and $\theta_{K,i} = \ln(K_{j,T_{ref}})$ to assure non-negative values of the pre-exponential factors according to the chemical theory. Activation energies and heats of adsorption are estimated by introducing a dimensionless energy parameter $\theta_{E,j} = \frac{E_{A,j}}{\Re \cdot T_{ref}}$ and $\theta_{H,i} = \frac{\Delta H_i}{\Re \cdot T_{ref}}$, respectively.

Due to the fact that the beginning and the end of the plate had a thicker catalyst layer and that at higher temperatures hotspot occurred, only the gas concentrations measured at positions that had a temperature deviation within (±2.5 K) were used for the parameter

estimation. By doing so, possible influences of pore diffusion and non-isothermicity on the kinetic parameters were minimized. For the determination of the kinetic parameters, data points of all isothermal temperature levels were evaluated simultaneously by Bayesian estimation using the software package Athena Visual Studio®, developed by Stewart and Caracotsios [63]. Stewart et al. showed that the method of least squares is not suitable for multiresponse data analysis unless the responses have known relative precisions and independent normal distributions of their errors [63,64]. The Bayesian estimation approach uses the prior knowledge of the experimenter (in the present case: the error range determined by replicate experiments) and gives a probability distribution called likelihood function of the parameters instead of a point estimate [65]. The likelihood function describes the probability for the model to generate the measured response values.

4.3.1. Results of the parameter estimation and discrimination

The parameter estimation shows two main results:

(1) In all models, the hydrogen adsorption constant K_{H_2} could not be estimated. That might indicate that the hydrogen adsorption did not influence the reaction rates significantly.
(2) The CO adsorption constant K_{CO} of models 5–16 could not be determined. The RDS in models 5–16 did not include an adsorbed CO. This means that the surface coverage of CO is negligible, as the reaction to form the carbon surface species is very fast, which is considered in the assumed rate-determining step.

The model discrimination was based on a simplified form of the Bayesian information criterion (BIC) developed by Schwarz [66]. The BIC takes the maximum likelihood function and the number of parameters to be estimated (n_P) and data-points (n_{DP}) into account. Akaike [67] showed that under the assumption of normally distributed errors, the sum of squares of the residuals (RSS) can be used.

$$\mathrm{BIC} = n_{DP} \cdot \ln\left(\frac{\mathrm{RSS}}{n_{DP}}\right) + n_P \cdot \ln(n_{DP}) \tag{24}$$

Comparing all the estimated models, the model with the lowest value of BIC is to be preferred. Due to the fact that all models have the same number of parameters ($n_P = 10$) and data-points ($n_{DP} = 7500$), the best model is the one with the lowest value of the sum of squares of the residuals.

The result of the model discrimination shows that the models 12b, 14b, and 6b gave the best fit to the experimental data over the temperature range from 280 to 360 °C. The estimated parameters are summarized in Table 6 for models 12b, 14b, and 6b, respectively. In addition to the best-fit values, the highest posterior density (HDP) intervals and the sum of squares of the residuals (RSS) are shown in this table. The highest posterior density interval defines the region in which 95% of the potential values of the parameters lie [63]. In the Supplementary material, the normalized covariance matrices of the three models are summarized, see Tables S1–S3. The elements in the covariance matrix E_{ij} are within the interval [−1, 1]; where a value of +1 (−1) indicates a strong correlation (anti-correlation) between parameter i and j.

The rate equations for the methanation and water gas shift reaction for model 12b with the assumed RDS ($C^* + H^* \rightarrow CH^* + *$) are shown in Eqs. (25) and (26), respectively

$$r_1 = \frac{k_1 \cdot K_C \cdot p_{CO}^{0.5} \cdot p_{H_2}^{0.5}}{(1 + K_C \cdot p_{CO} + K_{OH} \cdot p_{H_2O} \cdot p_{H_2}^{-0.5})^2} \tag{25}$$

$$r_2 = \frac{k_2 \cdot (K_\alpha \cdot p_{CO} \cdot p_{H_2O} - \frac{p_{CO_2} \cdot p_{H_2}}{K_{eq}})}{p_{H_2}^{0.5} \cdot (1 + K_C \cdot p_{CO} + K_{OH} \cdot p_{H_2O} \cdot p_{H_2}^{-0.5})^2} \tag{26}$$

Table 6
Kinetic parameters estimated for model 12b, 14b, and 6b.

	Model 12b 95% HPD intervals	Model 14b 95% HPD intervals	Model 6b 95% HPD intervals
$\ln k_1(T_{ref})$	0.15 ± 0.02	0.08 ± 0.01	0.042 ± 0.008
$\ln K_{OH}(T_{ref})$	−0.41 ± 0.05	−0.40 ± 0.06	−0.53 ± 0.06
$\ln K_{Cy}(T_{ref})$	0.57 ± 0.06	0.93 ± 0.04	2.58 ± 0.02
$\ln k_2(T_{ref})$	2.0 ± 0.07	2.12 ± 0.06	2.46 ± 0.05
$E_{A1}/(\Re T_{ref})$	14.9 ± 0.5	12.7 ± 0.3	11.8 ± 0.2
$\Delta H_{OH}/(\Re T_{ref})$	−14.6 ± 1.0	−17.6 ± 1.0	−19.8 ± 1.1
$\Delta H_{Cy}/(\Re T_{ref})$	−12.3 ± 0.4	−10.2 ± 0.4	1.3 ± 0.6
$E_{A2}/(\Re T_{ref})$	32.5 ± 1.2	31.3 ± 1.2	33.0 ± 1.1
$\ln K_\alpha(T_{ref})$	−1.07 ± 0.06	−1.02 ± 0.05	−1.04 ± 0.05
$\Delta H_\alpha/(\Re T_{ref})$	−1.3 ± 1.4	−0.35 ± 1.4	3.0 ± 1.1
RSS	757.6	775.8	777.3

The rate equations for the methanation and water gas shift reaction for model 14b with the assumed RDS ($CH^* + H^* \rightarrow CH_2^* + *$) are shown in Eqs. (27) and (28), respectively.

$$r_1 = \frac{k_1 \cdot K_{CH} \cdot p_{CO}^{0.5} \cdot p_{H_2}}{(1 + K_{CH} \cdot p_{CO}^{0.5} \cdot p_{H_2}^{0.5} + K_{OH} \cdot p_{H_2O} \cdot p_{H_2}^{-0.5})^2} \tag{27}$$

$$r_2 = \frac{k_2 \cdot \left(K_\alpha \cdot p_{CO} \cdot p_{H_2O} - \frac{p_{CO_2} \cdot p_{H_2}}{K_{eq}}\right)}{p_{H_2}^{0.5} \cdot (1 + K_{CH} \cdot p_{CO}^{0.5} \cdot p_{H_2}^{0.5} + K_{OH} \cdot p_{H_2O} \cdot p_{H_2}^{-0.5})^2} \tag{28}$$

The rate equations for the methanation and water gas shift reaction for model 6b with the assumed RDS ($COH^* + H^* \rightarrow CH^* + OH^*$) are shown in Eqs. (29) and (30), respectively.

$$r_1 = \frac{k_1 \cdot K_{COH} \cdot p_{CO} \cdot p_{H_2}}{(1 + K_{COH} \cdot p_{CO} \cdot p_{H_2}^{0.5} + K_{OH} \cdot p_{H_2O} \cdot p_{H_2}^{-0.5})^2} \tag{29}$$

$$r_2 = \frac{k_2 \cdot \left(K_\alpha \cdot p_{CO} \cdot p_{H_2O} - \frac{p_{CO_2} \cdot p_{H_2}}{K_{eq}}\right)}{p_{H_2}^{0.5} \cdot (1 + K_{COH} \cdot p_{CO} \cdot p_{H_2}^{0.5} + K_{OH} \cdot p_{H_2O} \cdot p_{H_2}^{-0.5})^2} \tag{30}$$

All three models assume the RDS to be the reaction of the surface carbon species (i.e., C^*, CH^*, or COH^*) with a strongly adsorbed hydrogen atom (H^*), and water to be adsorbed as a hydroxyl species (OH^*). These three models have an RSS significantly smaller than all the other models. The RSS values of the other models are up to 32% larger. Yet, it is difficult to favor one of these models, because the RSS of these three models are statistically equal; the deviation of the RSS values is less than 2.5%. On the one hand, model 12b has a slightly smaller value of RSS than the other two ($RSS_{12b} = 757.6$ compared to $RSS_{14b} = 775.8$ and $RSS_{6b} = 777.3$), but on the other hand, model 12b has a higher correlation between the parameters $\ln k_1(T_{ref})$ and $E_{A1}/(\Re T_{ref})$ and between $\ln k_2(T_{ref})$ and $E_{A2}/(\Re T_{ref})$ compared to the other two models, see covariance matrices in Tables S1–S3 in the Supplementary materials.

The activation energy of the methanation and water gas shift reactions for model 12b are 74.1 kJ/mol and 161.6 kJ/mol, respectively. The first value is close to the activation energy determined under similar experimental conditions by Gardner and Bartholomew et al. [9] 72–78 kJ/mol, McCarty and Wise [54] 71 kJ/mol and Hayes et al. [26] 78 kJ/mol, which assume the hydrogenation of adsorbed carbon as the rate-limiting step. The adsorption constants of the intermediate C^* and OH^* species satisfy the van't Hoff equation; the heats of adsorption are −60.9 kJ/mol and −72.3 kJ/mol, respectively. The value of the activation energy for the water gas shift reaction is difficult to compare with values from the literature, as the value is a lumped parameter containing the activation energy and the heat of adsorption of hydrogen and carbon dioxide.

A comparison between measured and calculated data shows that for H_2, the measured and calculated gas concentrations are in excellent agreement over the whole concentration range of

23–70 vol%. The values for CO, CO_2, CH_4 and H_2O are also in very good agreement, although the deviations for very small concentrations (less than ca. 5 vol%) exceed a limit of ±10%. A parity plot of the model results can be found in the Supplementary material, see Fig. S2.

In summary, the mathematical description of the channel reactor based on a one-dimensional model together with the rate equations of the models 12b, 14b, and 6b give a very good representation of the observed experimental data. The model can predict the concentration profiles of the different species along the reactor for all experimental conditions with high accuracy.

4.3.2. Comparison with a 1D model including axial dispersion

Fig. 14 shows the results of the one-dimensional model, which considers the axial dispersion in the bulk gas phase. The kinetic parameters for that model were determined with the one-dimensional model neglecting the axial dispersion as described earlier (Eqs. (6)–(8)). Fig. 14a and b depicts the measured and calculated gas concentration profiles at 280 °C for experiment nos. 1 and 7, respectively. Fig. 14c and d depicts the measured and calculated gas concentration profiles at 320 °C for experiment nos. 11 and 6, respectively. Fig. 14e and f depicts the measured and calculated gas concentration profiles at 360 °C for experiment nos. 10 and 4, respectively. The data from Fig. 14f were acquired on the catalyst plate no. 3, which has only 57 mg of catalyst on the metal plate, whereas all the other data shown were obtained on the catalyst plate no. 1. As noted earlier, only the isothermal region of the catalyst plate was modeled. Due to this fact, at 320 and 360 °C the models start from the axial position 11 and 31 mm, respectively. It is worth mentioning that all the kinetic parameters were determined by a one-dimensional model *excluding* axial dispersion, see Eqs. (6) and (7). Nevertheless, the predicted gas concentrations agree very well with the measured data over the wide range of temperatures and partial pressures. In the considered isothermal interval, the axial dispersion does not greatly influence the data and thus does not falsify the kinetic parameters.

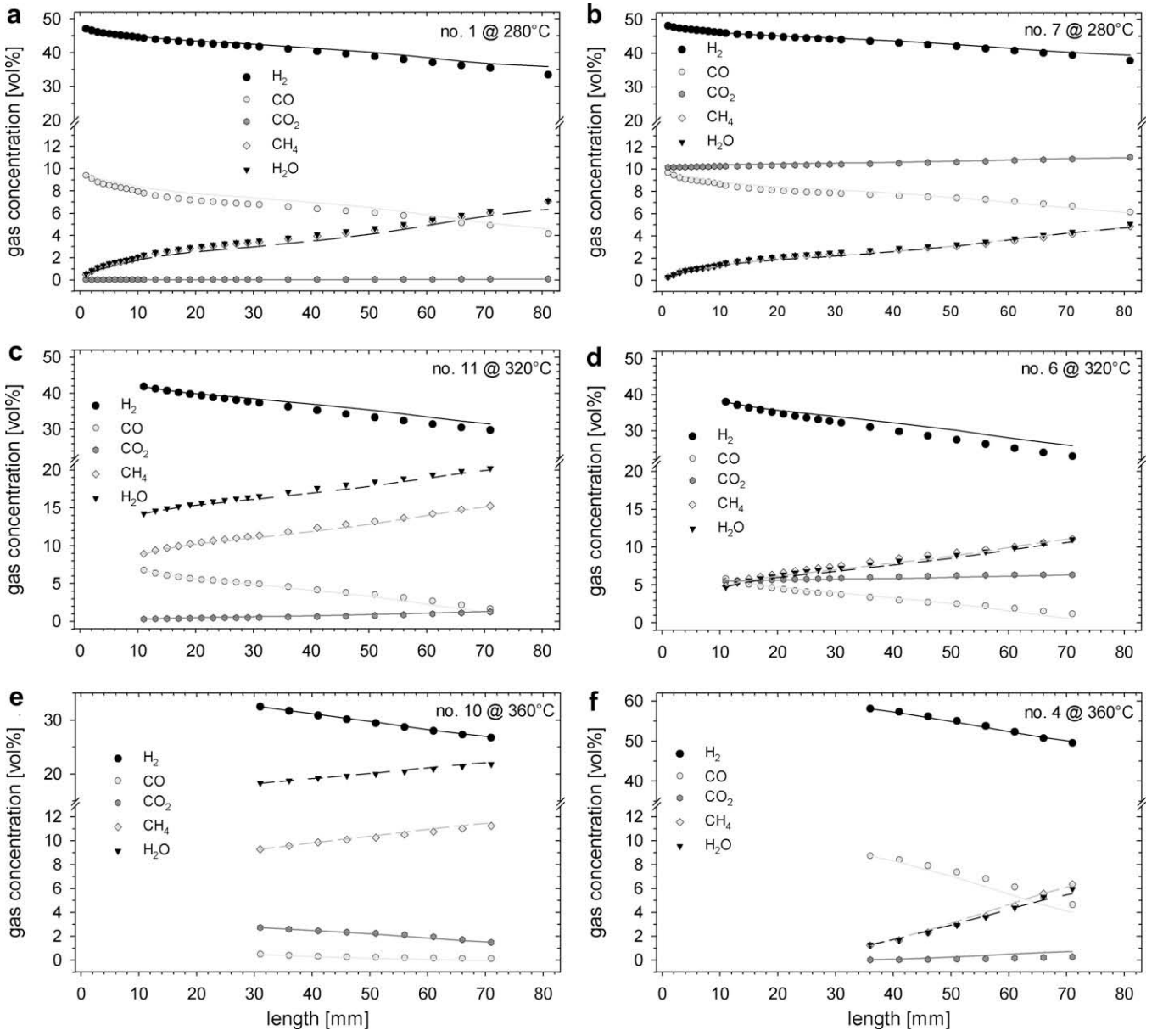

Fig. 14. Measured and calculated gas concentrations for various experiments at 280, 320, and 360 °C. The symbols (●) H_2, (◆) CH_4, (▼) H_2O, (○) CO, and (●) CO_2 refer to the experimental data, and lines are the results of a one-dimensional model considering the axial dispersion and including the kinetic parameters from model no. 12b determined with a one-dimensional model without axial dispersion.

4.4. Mass transfer influences

An important aspect in kinetic investigations is the mass transfer influence on the concentration data and thus on the kinetic parameters. In the catalytic plate reactor, bulk and pore diffusion limitation may occur under certain circumstances. In the following section, the influences of the diffusion limitation are evaluated for 280 and 360 °C (boundaries of the studied temperature range) by choosing CO as the reference gas species, due to its lower diffusion coefficient compared to that of hydrogen.

The Damköhler number (Da_{II}) describes the ratio of the chemical reaction rate to the maximum mass transfer rate. However, this requires the knowledge of the intrinsic reaction rate and of the external effectiveness number (η_e). Therefore, Carberry [68] introduced a modified Damköhler number considering the observed rate (r_{eff}) as shown in Eq. (31).

$$Ca = \eta_e \cdot Da_{II} = \frac{r_{eff}}{K_{G,i} \cdot a \cdot c_{b,i}} \tag{31}$$

Based on the one-dimensional model approach, the Carberry number (Ca) can be directly derived from Eq. (7) as the ratio of the observed chemical rate to the maximum mass transfer term in which $c_{s,i} = 0$, see Eq. (32). The mass transfer term is described by a Sherwood number as discussed earlier.

$$Ca = \frac{l_{ch} \cdot \omega_{cat} \cdot R_i}{b \cdot Sh \cdot D_{mix,i} \cdot c_{b,i}} \tag{32}$$

Fig. 15a and b shows the Carberry number for CO at 280 and 360 °C, respectively. At low temperature, no influence of bulk diffusion is observed ($Ca = 0.05$). At 360 °C, the Carberry number reaches values of around 0.24 and by this, the external effectiveness factor is approximately 0.8–0.9 for reactions with reaction orders between 0 and 1, as cited in [69].

A two-dimensional model without axial dispersion was solved by applying the kinetic parameters of model no. 12b. This two-dimensional model yields the species concentration profiles along both the height (y-axis) and the length (x-axis) of the channel reactor. This information was used to compare the true concentration distribution over the reactor height with the average gas concentration. The mass balances for the gas phase of the two-dimensional model are:

$$0 = \rho \cdot u_x(h) \cdot \frac{\partial w_i}{\partial x} - \frac{\partial}{\partial y}\left(\rho \cdot D_{i,mix} \frac{\partial w_i}{\partial y}\right) \tag{33}$$

The mass fraction w_i can be used here equivalent to the molar fraction x_i as the two are connected by the ratio of the molar mass of species i (M_i) to the average molar mass (M_{av}), and the total concentration c is replaced in Eq. (33) by the density of the gas mixture

$$\rho_{av} = M_{av} \frac{p}{R \cdot T} \tag{34}$$

The density of the gas mixture (ρ_{av}) contains the average molar mass (M_{av}), while the molar mass (M_i) of the considered species is constant and would show up in both terms of Eq. (33) and can therefore be divided out.

The continuity equation is:

$$\frac{\partial(\rho_{av} \cdot u_{av})}{\partial x} = 0 \tag{35}$$

The parabolic velocity profile u_x(h) is given by

$$u_x(h) = u_{av} \cdot 1.5\left(1 - \left(\frac{y - H/2}{H/2}\right)^2\right) \tag{36}$$

The boundary conditions are:

$$\begin{aligned} &\text{initial condition } x = 0 && w_i|_{x=0} = w_{i,feed} \\ &\text{outlet condition } x = L && \tfrac{\partial w_i}{\partial x}|_{x=L} = 0 \end{aligned} \tag{37}$$

$$\begin{aligned} &\text{quartz glass } y = H && \tfrac{\partial w_i}{\partial y}|_{y=H} = 0 \\ &\text{catalyst surface } y = 0 && \rho \cdot D_{i,mix} \cdot \tfrac{\partial w_i}{\partial y}|_{y=0} = \sum \nu_{ij} \cdot r_j \cdot M_i \end{aligned} \tag{38}$$

The average gas concentration for species i is calculated via:

$$x_{av} = \frac{\int_0^H u_x(h) \cdot x_i \cdot dy}{u_{av} \cdot H} \tag{39}$$

Figs. 16 and 17 show the height concentration profiles of CO at different axial positions in relation to the calculated average gas concentration for the same experiment at 280 and 360 °C, respectively. First, it can be seen that the average CO concentration of the profile is reached approximately 2 mm above the catalyst plate for both cases at every axial position. The gas-sampling capillary is placed approximately 1.5–2.3 mm above the catalyst surface (see gray bar in Figs. 16 and 17); the gas sample taken within this volume thus represents the average gas concentration. This is a necessary pre-requisite for the kinetic data acquired in this setup to be determined with a one-dimensional model using an average bulk gas concentration.

A further observation from the two-dimensional model is that the difference between the concentrations at the quartz plate and at the surface of the catalyst plate decreases along the reactor axis, and increases for higher temperatures. The profiles at 360 °C at the axial position 2 and 10 mm show that the surface concentration of CO is much lower than the bulk concentration. This effect is correctly taken into account in the one-dimensional model as well.

To estimate the influence of pore diffusion the Weisz modulus Ψ was calculated [70], which is based on the observed rates:

$$\Psi = \eta \cdot \Phi^2 \tag{40}$$

$$\Psi = \frac{l_{ch}^2 \cdot R_i}{D_{eff,i} \cdot c_{s,i}} \tag{41}$$

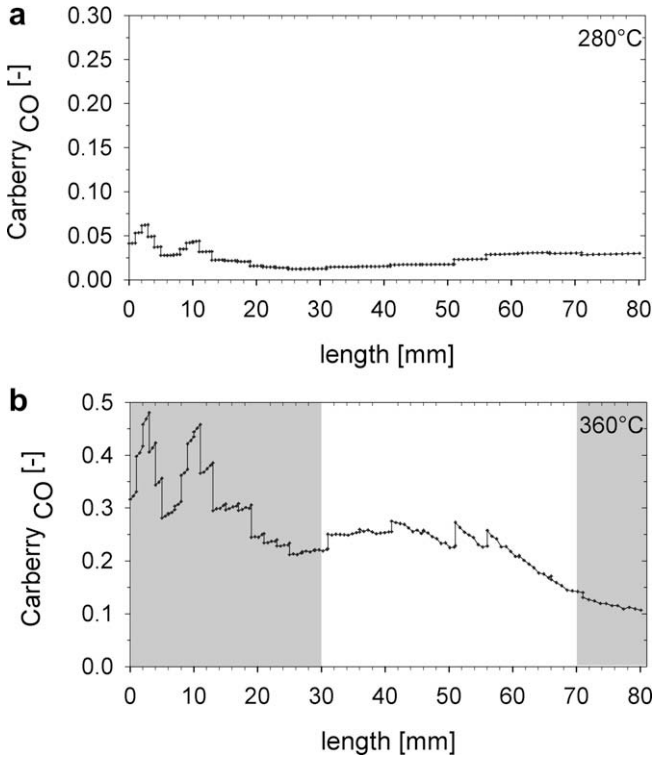

Fig. 15. Carberry number of CO (a) for 280 and (b) for 360 °C. The gray parts indicate the areas that were not used for the estimation of the kinetic parameters.

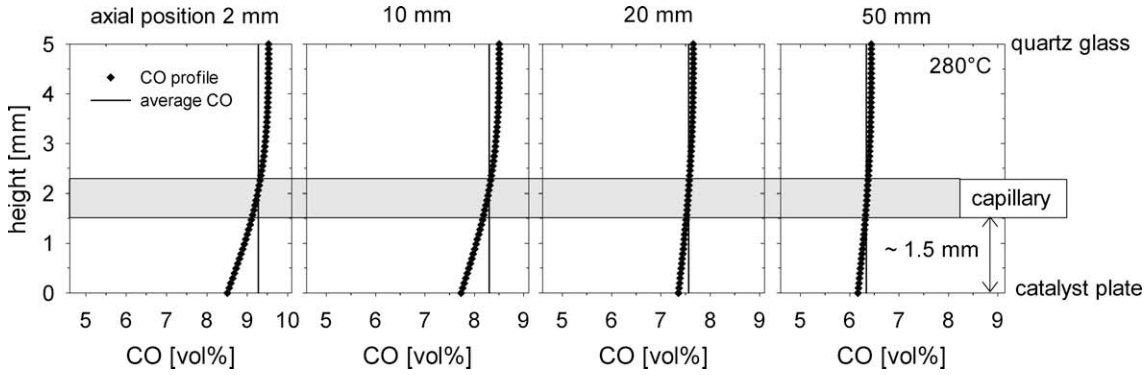

Fig. 16. Calculated CO concentration profiles over the channel height compared to the average CO concentration (vertical line) at the axial position 2, 10, 20, and 50 mm at 280 °C.

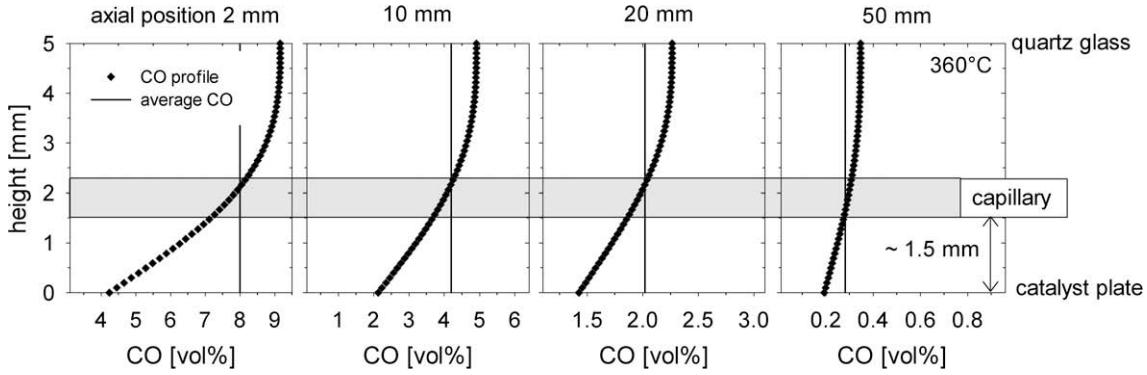

Fig. 17. Calculated CO concentration profiles over the channel height compared to the average CO concentration (vertical line) at the axial position 2, 10, 20, and 50 mm at 360 °C. Note that the scale of the *x*-axis changes from graph to graph.

where l_{ch} (m) is the characteristic length, R_i (mol m_{cat}^{-3} s^{-1}) the observed reaction rate of species i, $c_{S,i}$ (mol m^{-3}) the concentration on the external surface of the catalyst, and $D_{eff,i}$ (m^2 s^{-1}) is the effective diffusion coefficient of species i in the catalyst pores. D_{eff} is estimated by

$$D_{eff,i} = \frac{\varepsilon}{\tau}\left(\frac{1}{D_{i,mix}} + \frac{1}{D_{K,i}}\right)^{-1} \quad (42)$$

where the Knudsen diffusion coefficient $D_{K,i}$ is given by [71]:

$$D_{K,i} = 97 \cdot \frac{d_{pore}}{2} \cdot \sqrt{\frac{T_{cat}}{M_i}} \quad (43)$$

The values for the porosity and the tortuosity were set as $\varepsilon = 0.57$ and $\tau = 4.0$, respectively [70]. Using these equations, the effective diffusion coefficient and Weisz moduli for each gas species were calculated along the catalyst plate. The characteristic length was taken as the ratio of catalyst volume to surface. The plate was coated with catalyst particles of less than 45 μm with a given particle sphericity ϕ_P (confidential). Thus, the characteristic length l_{ch} is calculated as $(d_p \cdot \phi_P)/6$. Since the particles are coated onto the plate, it can be assumed that only half of the outer surface area is directly available for the gas on average; therefore, the characteristic length increases to $(d_p \cdot \phi_P)/3$. Pore diffusion can be neglected if the Weisz modulus Ψ is less than 0.15 [70]. Fig. 18a and b illustrates the Weisz modulus calculated for CO along the catalyst plate for 280 and 360 °C, respectively.

At temperatures below 340 °C, pore diffusion can be neglected, but above 360 °C it may have an influence on the observed rate, especially in the first 30 mm (see the gray part of Fig. 18b). In this

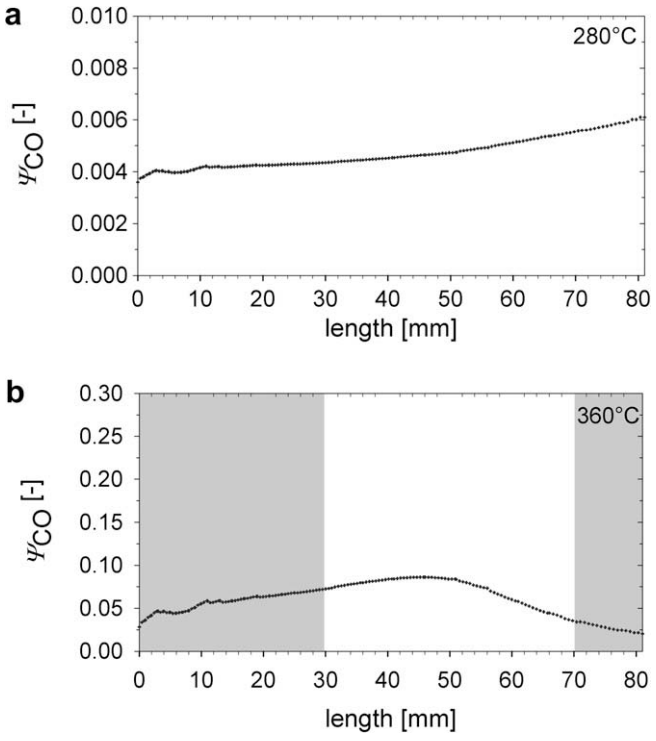

Fig. 18. Weisz modulus of CO (a) for 280 and (b) for 360 °C. The gray part indicates the areas that were not used for the estimation of the kinetic parameters.

area, also the temperature hotspots due to the higher catalyst mass occurred. By excluding the concentration data from axial positions within the hotspot for the determination of the kinetic parameters, the data affected by pore diffusion were excluded as well.

5. Conclusions

An extensive experimental study on the methanation and water gas shift reaction was carried out on a commercial nickel catalyst in a catalytic plate reactor over a wide range of temperatures and partial pressures. By means of spatially resolved measurements of the axial gas species concentrations and temperatures along the catalyst plate, the effects of reactants (H_2, CO) and products (CH_4, H_2O, CO_2) on the rates were analyzed. With this technique, a significantly larger set of data for the parameter estimation was collected than by use of a typical steady-state integral reactor with concentration measurements at the outlet only. Reaching chemical equilibrium at the reactor outlet was not a limitation for the kinetic analysis.

At temperatures above 340 °C, pore diffusion limitation may occur in the first few millimeters of the catalytically coated area; however, by applying axial gas concentration measurements, these data points could be safely excluded from the data set used for the parameter estimation. It can be summarized that the applied catalytic plate reactor with spatially resolved measurements is suitable for the kinetic study of heterogeneously catalyzed reactions such as methanation and the water gas shift reaction.

A one-dimensional reactor model including a generalized Langmuir–Hinshelwood rate expression was developed for the kinetic parameter estimation performed following Bayes' theorem. The predicted model results are in excellent agreement with the experimental data. By solving a two-dimensional model, it was shown that the measured gas concentration reflected the average gas concentrations used in the one-dimensional model. Furthermore, by solving a one-dimensional model including axial dispersion it was shown that in the considered isothermal interval axial dispersion does not greatly influence the data. Thus, the simpler one-dimensional model was sufficient to accurately estimate Langmuir–Hinshelwood parameters (pre-exponential factors, activation energies, and heats of adsorption) of the methanation and water gas shift reaction. The activation energy of the methanation reaction was 74 kJ/mol, which is consistent with values reported in the literature determined for similar conditions.

However, with this comprehensive data set and broad range of experimental condition, it was not possible to determine unambiguously the rate-limiting step for the considered reaction network. Three kinetic model approaches (nos. 12b, 14b, and 6b) corresponding to three different rate-determining steps reflected the measured data equally well. However, all three models include the hydrogenation of a carbonaceous intermediate as the rate-limiting surface reaction. Further discrimination of the models would require transient experiments [72] and/or spectroscopic methods such as in situ DRIFTS [73]. An optimized version of the channel reactor allowing higher system pressures (i.e., up to 20 bar_{abs} or higher) would be advantageous for a better model discrimination. Using such a setup, a series of experiments with constant feed gas composition but at different total pressures could be conducted. This would allow the dependencies on the total pressure of the different kinetic models to be investigated.

Acknowledgments

The financial support of Novatlantis is gratefully acknowledged. The authors thank P. Hottinger, T. Marti, E. De Boni, M. Hottiger, J. Schneebeli and T.-B. Truong for technical assistance, T. Lippert for profilometry and J. Mantzaras and S. Stucki for fruitful discussions.

Appendix A. Supplementary material

Supplementary data associated with this article can be found, in the online version, at doi:10.1016/j.jcat.2010.02.008.

References

[1] P. Sabatier, J.B. Senderens, Acad. Sci. 314 (1902) 514.
[2] M. Greyson, J.J. Demeter, M.D. Schlesinger, G.E. Johnson, J.Jonakin, J.W. Myers, Synthesis of Methane, Technical Report, Bureau of Mines, Report of Investigation 5137, Department of the Interior, 1955.
[3] G.A. Mills, F.W. Steffgen, Catal. Rev. 8 (1974) 159.
[4] M.A. Vannice, Catal. Rev. 14 (1976) 153.
[5] V. Ponec, Catal. Rev. Sci. Eng. 18 (1978) 151.
[6] C.H. Bartholomew, Catal. Rev. Sci. Eng. 24 (1982) 67.
[7] J.R.H. Ross, Metal Catalysed Methanation and Steam Reforming, Catalysis, vol. 7, Royal Society of Chemistry, 1985. pp. 1–45.
[8] J. Kopyscinski, T.J. Schildhauer, S.M.A. Biollaz, Fuel (2010), in press, doi:10.1016/j.fuel.2010.01.027.
[9] D.C. Gardner, C.H. Bartholomew, Ind. Eng. Chem. Prod. Res. Dev. 20 (1981) 80.
[10] D.C. Gardner, C.H. Bartholomew, Ind. Eng. Chem. Fundam. 20 (1981) 229.
[11] J. Klose, Reaktionskinetische Untersuchungen zur Methanisierung von Kohlenmonoxid, PhD thesis, Ruhr-Universität Bochum, Germany, 1982.
[12] E.L. Sughrue, C.H. Bartholomew, Appl. Catal. 2 (1982) 239.
[13] J. Klose, M. Baerns, J. Catal. 85 (1984) 105.
[14] Z.A. Ibraeva, N.V. Nekrasov, V.I. Yakerson, B.S. Gudkov, E.Z. Golosman, Z.T. Beisembaeva, S.L. Kiperman, Kinet. Catal. 28 (1987) 386.
[15] H. Chen, A.A. Adesina, J. Chem. Technol. Biotechnol. 60 (1994) 103.
[16] J. Sehested, S. Dahl, J. Jacobsen, J.R. Rostrup-Nielsen, J. Phys. Chem. B 109 (2005) 2432.
[17] W.W. Akers, R.R. White, Chem. Eng. Prog. 44 (1948) 553.
[18] P. Schoubye, J. Catal. 14 (1969) 238.
[19] T. Van Herwijnen, H. Van Doesburg, W.A. De Jong, J. Catal. 28 (1973) 391.
[20] M.A. Vannice, J. Catal. 37 (1975) 462.
[21] D.A. Saletore, W.J. Thomson, Ind. Eng. Chem. Process Des. Dev. 16 (1977) 70.
[22] S.V. Ho, P. Harriott, J. Catal. 64 (1980) 272.
[23] R.Z.C. van Meerten, J.G. Vollenbroek, M.H.J.M. de Croon, P.F.M.T. van Nisselrooy, J.W.E. Coenen, Appl. Catal. 3 (1982) 29.
[24] H. Inoue, M. Funakoshi, J. Chem. Eng. Jpn. 17 (1984) 602.
[25] T. Kai, S. Furusaki, K. Yamamoto, J. Chem. Eng. Jpn. 17 (1984) 280.
[26] R.E. Hayes, W.J. Thomas, K.E. Hayes, J. Catal. 92 (1985) 312.
[27] P. Biloen, Y. Soong, Transient Kinetic Study of Nickel Catalyzed Methanation: Final Report, University of Pittsburgh, 1986.
[28] A. Erhan Aksoylu, Z. ilsen Onsan, Appl. Catal. A 164 (1997) 1.
[29] R. Horn, K.A. Williams, N.J. Degenstein, L.D. Schmidt, J. Catal. 242 (2006) 92.
[30] R. Horn, N.J. Degenstein, K.A. Williams, L.D. Schmidt, Catal. Lett. 110 (2006) 169.
[31] R. Horn, K.A. Williams, N.J. Degenstein, L.D. Schmidt, Chem. Eng. Sci. 62 (2007) 1298.
[32] D. Dalle Nogare, N.J. Degenstein, R. Horn, P. Canu, L.D. Schmidt, J. Catal. 258 (2008) 131.
[33] B.C. Michael, A. Donazzi, L.D. Schmidt, J. Catal. 265 (2009) 117.
[34] M. Bosco, F. Vogel, Catal. Today 116 (2006) 348.
[35] M. Bosco, Kinetic Studies of the Autothermal Gasoline Reforming for Hydrogen Production for Fuel Cell Applications, PhD thesis, ETH Zurich, Switzerland, 2006 (Diss. ETH No. 16865).
[36] J. Mantzaras, R. Bombach, R. Schaeren, Proc. Combust. Inst. 32 (2009) 1937.
[37] FLIR Systems Indigo Operations, Alpha NIR User's Guide Version 150.
[38] Herasil®, Heraeus Quarzglass GmbH & Co. KG, Heraeus Datasheet for quartz glass.
[39] C.P. Huang, J.T. Richardson, J. Catal. 51 (1978) 1.
[40] M.V. Ciocco, D.G. Blackmond, Appl. Catal. 44 (1988) 105.
[41] Dektak 8 Advanced Development Profiler Manual.
[42] R.E. Hayes, S.T. Kolaczkowski, Chem. Eng. Sci. 49 (1994) 3587.
[43] M. Zanfir, A. Gavriilidis, Chem. Eng. Sci. 56 (2001) 2671.
[44] L.L. Raja, R.J. Kee, O. Deutschmann, J. Warnatz, L.D. Schmidt, Catal. Today 59 (2000) 47.
[45] C.R. Wilke, J. Chem. Phys. 18 (1950) 517.
[46] B.E. Poling, J.M. Prausnitz, J.P. ÓConnell, The Properties of Gases and Liquids, fifth ed., McGraw-Hill, New York, 2001.
[47] M. Araki, V. Ponec, J. Catal. 44 (1976) 439.
[48] H. Inoue, M. Funakoshi, Int. Chem. Eng. 21 (1981) 276.
[49] J. Happel, I. Suzuki, P. Kokayeff, V. Fthenakis, J. Catal. 65 (1980) 59.
[50] J. Happel, H.Y. Cheh, M. Otarod, S. Ozawa, A.J. Severdia, T. Yoshida, V. Fthenakis, J. Catal. 75 (1982) 314.
[51] R.P. Underwood, C.O. Bennett, J. Catal. 86 (1984) 245.
[52] I. Alstrup, J. Catal. 151 (1995) 216.
[53] P.R. Wentrcek, B.J. Wood, H. Wise, J. Catal. 43 (1976) 363.
[54] J.G. McCarty, H. Wise, J. Catal. 57 (1979) 406.
[55] R. Yadav, R.G. Rinker, Ind. Eng. Chem. Res. 31 (1992) 502.

[56] V.M. Vlasenko, G.E. Yuzefovich, Russ. Chem. Rev. 38 (1969) 728.
[57] G.I. Golodets, Theor. Exp. Chem. 21 (1985) 525.
[58] J.W.E. Coenen, P.F.M.T. van Nisselrooy, M.H.J.M. de Croon, P.F.H.A. van Dooren, R.Z.C. van Meerten, Appl. Catal. 25 (1986) 1.
[59] M. Andersson, F. Abild-Pedersen, I. Remediakis, T. Bligaard, G. Jones, J. Engbaek, O. Lytken, S. Horch, J. Nielsen, J. Sehested, J. Rostrup-Nielsen, J. Norskov, I. Chorkendorff, J. Catal. 255 (2008) 6.
[60] V. Sanchez-Escribano, M. Larrubia Vargas, E. Finocchio, G. Busca, Appl. Catal. A 316 (2007) 68.
[61] J. Xu, G.F. Froment, AIChE J. 35 (1989) 88.
[62] Design Institute for Physical Properties, DIPPR Project 801 Full Version, 2005.
[63] W.E. Stewart, M. Caracotsios, Computer-aided Modeling of Reactive Systems, first ed., Wiley & Sons, New Jersey, 2008.
[64] W.E. Stewart, M. Caracotsios, J.P. Sorensen, AIChE J. 38 (1992) 641.
[65] S.-H. Hsu, S.D. Stamatis, J.M. Caruthers, W.N. Delgass, V. Venkatasubramanian, G.E. Blau, M. Lasinski, S. Orcun, Ind. Eng. Chem. Res. 48 (2009) 4768.
[66] G. Schwarz, Anal. Stat. 6 (1978) 461.
[67] H. Akaike, IEEE T. Automat. Contr. 19 (1974) 716.
[68] J.J. Carberry, Chemical and Catalytic Reaction Engineering, McGraw-Hill, New York, 1976.
[69] R.A. van Santen, P.W.N.M. van Leeuwen, J.A. Moulijn, B.A. Averill, Catalysis: An Integrated Approach, second ed., Elsevier/Netherlands Institute for Catalysis Research, Amsterdam, 1999.
[70] C.N. Satterfield, Mass Transfer in Heterogeneous Catalysis, MIT Press, London, 1970.
[71] R.E. Hayes, S.T. Kolaczkowski, Introduction to Catalytic Combustion, Gordon and Breach Science, 1997.
[72] T.R. Boehme, C.H. Onder, L. Guzzella, Int. J. Hydrogen Energy 33 (2008) 6150.
[73] E.E. Ortelli, J. Wambach, A. Wokaun, Appl. Catal. A 192 (2000) 137.